

AD A108881

12
LEVEL

AFGL-TR-81-0252

THE DEVELOPMENT AND TESTING OF METHODS TO INFER MIDLATITUDE
PRECIPITATION INTENSITY FROM GEOSYNCHRONOUS SATELLITE INFRARED DATA

John V. Zapotocny
Donald R. Johnson
Thomas M. Whittaker

Space Science & Engineering Center
University of Wisconsin
1225 West Dayton Street
Madison, Wisconsin 53706

31 July 1981

Scientific Report No. 3

Approved for public release; distribution unlimited

AIR FORCE GEOPHYSICS LABORATORY
AIR FORCE SYSTEMS COMMAND
UNITED STATES AIR FORCE
HANSCOM AFB, MASSACHUSETTS 01731

DTIC
ELECTE
S DEC 28 1981 D
D

8112 2807

DTIC FILE COPY

Qualified requestors may obtain additional copies from the Defense Technical Information Center. All others should apply to the National Technical Information Service.

Unclassified

SECURITY CLASSIFICATION OF THIS PAGE (When Data Entered)

REPORT DOCUMENTATION PAGE		READ INSTRUCTIONS BEFORE COMPLETING FORM
1. REPORT NUMBER AFGL-TR-81-0252	2. GOVT ACCESSION NO. AD-A108 881	3. RECIPIENT'S CATALOG NUMBER
4. TITLE (and Subtitle) THE DEVELOPMENT AND TESTING OF METHODS TO INFER MIDLATITUDE PRECIPITATION INTENSITY FROM GEOSYNCHRONOUS SATELLITE INFRARED DATA		5. TYPE OF REPORT & PERIOD COVERED Scientific Report No. 3
7. AUTHOR(s) John V. Zapotocny Donald R. Johnson Thomas M. Whittaker		6. PERFORMING ORG. REPORT NUMBER
9. PERFORMING ORGANIZATION NAME AND ADDRESS Space Science and Engineering Center, Univ. of Wi. 1225 West Dayton Street Madison, WI 53706		8. CONTRACT OR GRANT NUMBER(s) D19628-78-C-0137
11. CONTROLLING OFFICE NAME AND ADDRESS Air Force Geophysics Laboratory Hanscom Air Force Base, MA 01731 Monitor/R.S. Hawkins/LYU		10. PROGRAM ELEMENT, PROJECT, TASK AREA & WORK UNIT NUMBERS 62101F 667008AB
14. MONITORING AGENCY NAME & ADDRESS (if different from Controlling Office)		12. REPORT DATE 31 July 1981
		13. NUMBER OF PAGES 90
		15. SECURITY CLASS. (of this report)
		15a. DECLASSIFICATION/DOWNGRADING SCHEDULE
16. DISTRIBUTION STATEMENT (of this Report) Approved for public release; distribution unlimited		
17. DISTRIBUTION STATEMENT (of the abstract entered in Block 20, if different from Report)		
18. SUPPLEMENTARY NOTES		
19. KEY WORDS (Continue on reverse side if necessary and identify by block number) GOES Satellite data, Precipitation intensity inference, weather analysis		
20. ABSTRACT (Continue on reverse side if necessary and identify by block number) GOES satellite IR brightness data were used in a pilot study to infer precipitation intensity and intensity changes due to convection embedded within continuous precipitation areas.		

SECURITY CLASSIFICATION OF THIS PAGE(When Data Entered)

BLANK PAGE

SECURITY CLASSIFICATION OF THIS PAGE(When Data Entered)

TABLE OF CONTENTS

	<u>Page</u>
Table of Contents	iii
List of Figures	iv
List of Tables	vii
1. Introduction	1
2. Background	4
3. Selection and description of synoptic cases	9
3.1 14 April 1980, central United States	9
3.2 6 February 1980, southeastern United States	11
3.3 2 March 1980, southeastern United States	13
3.4 31 January-1 February 1980, central United States	14
4. Data sample	16
5. Procedures for calculation of parameters	20
5.1 Selection of appropriate brightness arrays	20
5.2 Assignment of point brightness values	21
5.3 Calculation of the five parameters for selected arrays	21
5.4 Parameter categorization	24
6. Results	25
6.1 Comparison of snowfall parameters with observed snowfall intensity	25
6.2 Comparison of snowfall parameter changes with observed hourly snowfall intensity changes	32
6.3 Determination of the most skillful indicators for intensity and intensity change	34
6.4 Determining intensity change for the 50 array subset	37
7. Conclusions	40
References	44

Accession For	
NTIS GRA&I	<input checked="" type="checkbox"/>
DTIC TAB	<input type="checkbox"/>
Unannounced	<input type="checkbox"/>
Justification	
By	
Distribution/	
Availability Codes	
Dist	Avail and/or Special
A	

DTIC
ELECTE
S DEC 28 1981 **D**
D

LIST OF FIGURES

Figure

- 1 Typical distributions of mesoscale convective bands within occluded and developing cyclones.
- 2 NMC surface analyses for 1200 GMT 14 April 1980, 1800 GMT 14 April 1980 and 0000 GMT 15 April 1980.
- 3 NMC 500 mb geopotential analyses (heights in decameters) for 1200 GMT 14 April 1980 and 0000 GMT 15 April 1980.
- 4 Vertical temperature and dewpoint distributions for Peoria, Illinois and Green Bay, Wisconsin, 1200 GMT 14 April 1980.
- 5 SMS-II satellite imagery, visible and infrared, 1600 GMT 14 April 1980.
- 6 Same as Figure 5 except for 2300 GMT 14 April 1980.
- 7 Same as Figure 2 except for 1200 GMT 6 February 1980, 1800 GMT 6 February 1980 and 0000 GMT 7 February 1980.
- 8 Same as Figure 3 except for 1200 GMT 6 February 1980.
- 9 Same as Figure 4 except for Dulles International Airport, Maryland and Greensboro, North Carolina, 1200 GMT 6 February 1980.
- 10 Same as Figure 5 except for 1400 GMT 6 February 1980.
- 11 Same as Figure 5 except for 2100 GMT 6 February 1980.
- 12 Same as Figure 2 except for 1200 GMT 2 March 1980, 1800 GMT 2 March 1980 and 0000 GMT 3 March 1980.
- 13 Same as Figure 3 except for 1200 GMT 2 March 1980 and 0000 GMT 3 March 1980.
- 14 Same as Figure 4 except for Greensboro, North Carolina and Cape Hatteras, North Carolina, 1200 GMT 2 March 1980.

LIST OF FIGURES, cont.

Figure

- 15 Same as Figure 5 except for 1400 GMT 2 March 1980.
- 16 Same as Figure 5 except for 2100 GMT 2 March 1980.
- 17 Same as Figure 2 except for 1200 GMT 31 January 1981, 1800 GMT 31 January 1981 and 0000 GMT 1 February 1981.
- 18 Same as Figure 3 except for 1200 GMT 31 January 1981 and 0000 GMT 1 February 1981.
- 19 Same as Figure 4 except for Omaha, Nebraska, 1200 GMT 31 January 1981.
- 20 Example McIDAS listings of weather observations, 6 February 1980.
- 21 Sample digital infrared brightness array with mean, median, mode and standard deviation of array values.
- 22 Example of point brightness calculation.
- 23 Example showing magnitude dependency of Laplacian values upon the "circularity" of relative maxima or minima.
- 24 Example showing dependency of Laplacian values upon the orientation of banded maxima or minima.
- 25 Schematic of five point Laplacians (ILAP1 and OLAP1) and nine point Laplacians (ILAP2 and OLAP2) including equations used for calculations.
- 26 Tabulation format for hourly values of visibility, weather and all five parameters.
- 27 Tabulation format for hourly changes in visibility and all five parameters.
- 28 Interval frequency distributions of DM values for light and moderate, heavy snowfall occurrences.
- 29 Same as Figure 28 except for ILAP1 and OLAP1.
- 30 Same as Figure 28 except for ILAP2 and OLAP2.

LIST OF FIGURES, cont.

Figure

- 31 Madison, Wisconsin centered brightness arrays from 1900, 2000 and 2100 GMT 14 April 1980 superimposed on concurrent radar depictions.
- 32 Interval frequency distributions of ΔDM values for intensity decreases and intensity increases.
- 33 Same as Figure 32 except for $\Delta ILAP1$ and $\Delta OLAP1$
- 34 Same as Figure 32 except for $\Delta ILAP2$ and $\Delta OLAP2$.
- 35 Interval frequency difference distribution of DM, including subtotal frequency differences for positive and negative intervals, for light and moderate, heavy snowfall occurrences.
- 36 Same as Figure 35 except for ILAP1, OLAP1, ILAP2 and OLAP2.
- 37 Interval frequency difference distribution of ΔDM for intensity decreases and intensity increases. See Figure 35 for format.
- 38 Same as Figure 37 except for $\Delta ILAP1$, $\Delta OLAP1$, $\Delta ILAP2$ and $\Delta OLAP2$.
- 39 Interval frequency distributions of ΔDM for intensity decreases and intensity increases for special 50 array subset.
- 40 Same as Figure 39 except for $\Delta ILAP1$ and $\Delta OLAP1$.
- 41 Same as Figure 39 except for $\Delta ILAP2$ and $\Delta OLAP2$.
- 42 Same as Figure 37 except for special 50 array subset.
- 43 Same as Figure 42 except for $\Delta ILAP1$, $\Delta OLAP1$, $\Delta ILAP2$ and $\Delta OLAP2$.

LIST OF TABLES

<u>Table</u>		<u>Page</u>
1	Stations and hours for which data arrays were produced for 14 April 1980 case.	18
2	Same as Table 1 except for 6 February 1980 case.	18
3	Same as Table 1 except for 2 March 1980 case.	19
4	Same as Table 1 except for 31 January-1 February 1981 case.	19
5	Average values of all five parameters and visibility for each snowfall intensity category.	26
6	Hypothesized sign distribution of parameter averages for each snowfall intensity category.	26
7	Parameter averages and number of occurrences for each snowfall intensity category for individual synoptic cases.	28
8	Standard deviations of parameter values for each intensity category.	28
9	Average hourly changes in all parameters for each intensity change category.	33
10	Hypothesized sign distribution of average hourly parameter changes for each intensity change category.	33
11	Average hourly parameter changes for each intensity change category, for the special 50 array subset (standard deviation of brightness values >6.0).	38

BLANK PAGE

1. INTRODUCTION

In recent years, research has been conducted in the determination of precipitation intensity from geosynchronous satellite information. Studies by Sikdar¹, Stout, Martin and Sikdar², Schofield and Oliver³, and Adler and Fenn⁴ dealt specifically with determining convective rainfall rates in tropical areas using satellite infrared (IR) brightness data. The majority of this work has been related to inference of tropical convective precipitation with much less work being done to develop similar techniques for continuous precipitation areas in middle latitudes.

Convective bands or clusters imbedded within areas of less vertically developed stratiform cloudiness are commonly observed in the cold sector of rapidly deepening cyclones as well as mature occluded storms. These imbedded convective areas are nearly always associated with increased precipitation intensity relative to areas of surrounding stratiform cloudiness.

In an attempt to aid development of simple techniques applicable in middle latitudes, this study addresses the inference of

1. Sikdar, D. N., 1971: ATS-3 observed cloud brightness field related to a meso-to-synoptic scale rainfall pattern. Tellus, 24, 400-412.
2. Stout, J., D. Martin and D. N. Sikdar, 1979: Estimating rain with geosynchronous satellite images. Mon. Wea. Rev., 107, 585-598.
3. Schofield, R. A., and V. J. Oliver, 1977: A scheme for estimating convective rainfall from satellite imagery. NESS Tech. Memo. 86, NOAA, 47 pp.
4. Adler, R. F., and D. D. Fenn, 1978: Thunderstorm intensity as determined from satellite data. J. Appl. Meteor., 18, 502-517.

precipitation intensity and its temporal change associated with imbedded convective activity at a location in areas of continuous stratiform precipitation from Geosynchronous Operational Environmental Satellite (GOES) IR digital data.

Imbedded convective activity is easily identified in high resolution visible GOES imagery if high cloud layers are not present to obscure the convection. At low sun angles with the shadowing effect of the convective towers, details of these convective areas are especially enhanced. However, with the need for these methods to be applicable during both daytime and nighttime hours, only the IR 11 micron channel data were used in this study which was based on several synoptic cases. In each of the cases examined, visible and IR imagery and loops were used to help pinpoint optimum areas for study.

Arrays of digital IR brightness values were obtained through the Man-computer Interactive Data Access System (McIDAS) of the Space Science and Engineering Center at the University of Wisconsin-Madison.⁵ These arrays, approximately 36 nautical miles (nm) on a side with 324 data points each, were centered on surface observing stations which experienced highly variable precipitation intensity for a period of several hours during each case. Five numerical parameters were then computed from each array to test their utility for inference of precipitation intensity and change and to note any consistent

5. Wash, C. H., J. Stremikis and D. R. Johnson, 1979: Objective forecasts of subsynoptic convective areas using interactive computer systems. AMS Preprint Volume, 11th Conference on Severe Local Storms, 2-5 October 1979.

tendencies in the behavior of the parameters.

Only precipitation in the form of snow was considered since any intensity changes are easily detectable from changes in horizontal surface visibility. One obvious problem is the influence of blowing snow on the surface visibility. This effect, however, was considered less critical than the usual presence of fog and/or other obscurations in continuous rainfall cases which makes visibility less useful as an intensity indicator. Stations which exhibited considerable variability in snowfall intensity (visibility) were selected from four recent (1980-1981) snowstorm occurrences. A total of over 300 brightness arrays centered on these stations formed the data base for the study. The results of this research, with addition of several more cases and further refinement of the numerical parameters used, could aid in development of techniques for detection and very short range forecasting of rapid changes in snowfall intensity (visibility) using only GOES data and surface observations for information sources.

2. BACKGROUND

Since the advent of the meteorological satellite in the late 1950's, research has been directed towards the pioneering of new methods using satellite data and the improvement of older methods. This trend continues into the decade of the 1980's with large research efforts in the atmospheric sciences revolving around the use of satellite information. With the launching of the first geosynchronous operational satellite, SMS-II, in May of 1974, a breakthrough in satellite meteorology occurred with the capability to resolve the time evolution of atmospheric phenomena. Considerable applications have been developed for the use of GOES data. In addition to diagnosis and forecasting through viewing imagery, development of techniques has been completed for:

- 1) determining upper level wind structure from observed cloud motions⁶
- 2) estimating convective rainfall rates, from IR brightness data, in tropical convection⁷
- 3) indirectly sounding the temperature and moisture structure of the

6. Johnson, G. L., and D. Suchman, 1980: Intercomparisons of SMS wind sets: a study using rapid scan imagery. Mon. Wea. Rev., 108, 1672-1688.

7. Stout, J., D. Martin and D. N. Sikdar, 1979: Estimating rain with geosynchronous satellite images. Mon. Wea. Rev., 107, 585-598.

atmosphere⁸.

The work conducted in this study is most closely related to (2) except that the research deals with convection in mid-latitudes. A somewhat similar study conducted by Wylie⁹ attempted to apply techniques developed for estimating tropical convective precipitation rates¹⁰ to middle latitudes. These results indicated that, although estimated errors for these techniques were much larger in middle than tropical latitudes, the relative accuracy might be increased with additional parameterization through use of radiosonde data. Since the techniques were originally developed for convection in warm air masses, errors in the application of the tropical techniques to mid-latitudes also varied greatly between the summer and fall cases examined. Little additional work has been conducted either to apply already developed techniques or to develop new techniques for determination of mid-latitude precipitation solely from GOES data.

8. Smith, W. L., V. E. Suomi, W. P. Menzel, H. M. Woolf, L. A. Sromovsky, H. E. Revercomb, C. M. Hayden, D. N. Erickson and F. R. Mosher, 1981: First sounding results from VAS-D. Bull. Amer. Meteor. Soc., 62, 232-236.
9. Griffeth, C. G., W. L. Woodley, P. G. Grube, D. W. Martin, J. Stout and D. N. Sikdar, 1978: Rain estimation from geosynchronous satellite imagery-visible and infrared studies. Mon. Wea. Rev., 106, 1153-1171.
10. Griffeth, C. G., W. L. Woodley, P. G. Grube, D. W. Martin, J. Stout and D. N. Sikdar, 1978: Rain estimation from geosynchronous satellite imagery-visible and infrared studies. Mon. Wea. Rev., 106, 1153-1171.

Without question, a large amount of precipitation in mid-latitudes falls as continuous, stratiform type, rain or snow. Generally, the intensity of this type of precipitation is quite uniform with little short-term variation. However, convective activity is occasionally imbedded within areas of stratiform precipitation and under these circumstances very large temporal changes of intensity occur with the passage of convective cells over a particular locale. Often these enhanced precipitation events elude the synoptic reporting network and, except for radar, go undetected. The capability to remotely detect these events through the use of GOES data is highly desirable.

Typically, the convection imbedded within a mid-latitude storm system is located in the cold sector of the cyclone in the proximity of the surface cyclone center¹¹. It appears that this convective activity is primarily associated with either occluded cyclones or rapidly developing cyclones along the eastern coast of continents.¹² Figure 1 shows some typical storm structures and the convective patterns frequently observed in the cold sectors. Note the banded structure of the convection commonly associated with an occlusion and the cluster pattern usually observed in the coastal storms. One can suggest the following reasons for the preferred convective development with the occluded and coastal cyclones.

11. Hobbs, P. V., and J. D. Locatelli, 1978: Rainbands, precipitation cores and generating cells in a cyclonic storm. J. Atmos. Sci., 35, 230-241.
12. Houze, R. A., Jr., P. V. Hobbs, K. R. Biswas and W. M. Davis, 1976: Mesoscale rainbands in extratropical cyclones. Mon. Wea. Rev., 104, 868-878.

In the case of occluded storms, a primary forcing for the stratiform precipitation in and near the storm center is the ascent due to low level frictionally induced convergence. With the occlusion, a very cold pool of air aloft becomes located directly over the surface cyclone center and results in a minimum of static stability in the mid troposphere near the storm center. If sufficient frictional convergence is present to lift the moist air through the usually stable lower levels of the atmosphere, convective activity develops in the less stable layers of the mid troposphere. Rapidly deepening coastal cyclones are nearly always associated with intense Positive Vorticity Advection (PVA) aloft and upward vertical motion. This, combined with the readily available moisture supply of coastal locations and thus relatively high equivalent potential temperatures, likely triggers convection near the cyclone center where upper level divergence is maximized. A positive feedback results with the strong latent heat release forcing the enhancement of the convection.

The convective activity just described usually propagates with the middle level wind flow and persists for a period of several hours. As noted by previous investigators, these convective areas are readily evident in visible satellite imagery and usually are associated with bright areas in the IR imagery. Since the brightness of a radiating body in an IR satellite image, as conventionally displayed, is inversely proportional to the absolute temperature, a large brightness

value would imply a cold temperature¹³. The relative high brightness displayed by these imbedded convective areas requires that the cloud tops of the convection are significantly colder than the tops of the surrounding stratiform cloudiness, observations from aircraft indicate that the cloud tops are usually several thousands of feet higher than the stratiform cloud tops¹⁴. Due to the fact that many of these convective bands and clusters are very small, with typical radial dimensions of several miles, high resolution satellite data is required to detect the majority of the convective activity.

13. Brandli, H. W., 1976: Satellite Meteorology, Air Weather Service Tech. Rep., AWS-TI-76-264, Hq Air Weather Service, Scott AFB, II, 188 pp.

14. Brandli, op. cit.

3. SELECTION AND DESCRIPTION OF SYNOPTIC CASES

For the screening and selection of the SMS satellite information and hourly surface observations which formed the data base for this study, fifteen snowstorms during the winters of 1979-1980 and 1980-1981 were examined. In the screening, if surface visibility observations for several stations within a particular storm indicated variable snowfall intensity, SMS-II satellite information and surface observations were selected from the McIDAS satellite data archive. The imagery with 2nm resolution at subpoint was obtained at half-hour intervals over an eight-hour period for seven of the storms with variable snowfall intensity. The methods of obtaining the station-centered arrays of digital IR brightness values used for study and a detailed description of their structure are discussed in a later section.

Of the snowstorms examined, only four cases satisfied the requirement that the actual surface observations of variable visibility and the area of embedded convection evident in the satellite imagery were co-located. A brief synoptic description of these four cases selected for detailed study is now presented.

3.1 14 April 1980, Central United States.

The Midwest storm on 14 April 1980 was in a more developed stage than any of the other three cases which were studied. The system had occluded prior to this data period.

The Midwest cyclone of 14 April 1980 developed along the Louisiana Gulf coast early on the preceding day. At that time, a strong low level baroclinic zone was situated along the coast and a very high amplitude trough at upper levels was located over the central U. S. with an axis from Lake Winnepeg in southern Canada to southern Texas. Strong westerlies with a 110 knot wind maximum were located in the southern portion of the trough. The patterns of divergence and vorticity indicated that the atmospheric structure was ideal for the occurrence of surface cyclogenesis in the central Gulf coast states.

The surface cyclone deepened during its northerly movement with the central sea level pressure falling 8 mb in the 12 hour period ending 0000 GMT 14 April. At this time, the storm was centered in extreme northern Alabama. Occlusion was occurring rapidly during this period. Based on analyses from the National Meteorological Center (NMC), the storm was fully occluded by 1200 GMT 14 April (Figure 2). During the following 12 hours, the center continued to move slowly northward to a location in east central Illinois by 0000 GMT 15 April. The 500 mb flow during this stage of occlusion, 1200 GMT 14 April to 0000 GMT 15 April, was dominated by an expansive cold core closed low over the central U.S. The circular symmetry of the height contours shown in Figure 3 suggests that during this period the PVA was a minimum; hence, little further intensification of the storm occurred.

The significant snowfall during 14 April was confined to a narrow band from northeastern Arkansas to northern lower Michigan. Figure 2a

indicates the stations in this band over which brightness arrays for the study were centered. The embedded convective nature of the clouds in northern Illinois and southern Wisconsin within the snow band is evident from the satellite images shown in Figures 5 and 6. The convection is especially apparent in the visible images. Note that the large brightness values in the IR images are also coincident with these areas. Many of the banded convective areas persisted for several hours during their relative propagation around the circulation center. Strong low level convergence near the surface cyclone center combined with the unstable lapse rate shown in Figure 4 was likely a primary factor in the forcing of this convective activity.

3.2 6 February 1980, Southeastern United States.

The storm in the Southeastern United States on 6 February 1980 was a type very different from the Midwest storm that was just described. At the beginning of the satellite data period, 1400 GMT 6 February, a weak occluded cyclone that had been drifting slowly southeastward for several days accompanied by light precipitation was located in the lower Ohio River valley. At the same time, with favorable upper-level and lower-level baroclinic support along the Atlantic coast, cyclogenesis was occurring along the South Carolina coast. The primary precipitation area was associated with this newly-developed cyclone center.

In Figure 7, the development of the surface center off the coast was quite slow initially, but rapid deepening eventually occurred late

in the period of interest. The central sea level pressure dropped 14 mb in the six hours ending 0000 GMT 7 February. Eventually, the lowest pressure attained by the storm was 986 mb at 1200 GMT 7 February. The most significant snowfall associated with the new center was in a band from South Carolina northeastward through Washington, D.C.

The distribution of stations reporting variable snowfall intensities on the eastern slopes of the Appalachian chain, (Figure 7a), together with the predominantly easterly low level wind flow, suggests that orographically induced rising motion was partially responsible for the convective activity in the cold sector of this cyclone. Unlike the first case, this developing system was linked with a rather strong, fast-moving upper-level short wave disturbance. The strong PVA over the region of development indicated in the 500 mb chart (Figure 8) and the other NMC model analyses (not shown) likely also aided the convective development.

The visible and IR satellite images of Figures 10 and 11 show considerable cirrus cloudiness present throughout the data period (1400 GMT - 2100 GMT 6 February). The convective activity, though somewhat difficult to observe in visible and IR channels due to the presence of this cirrus, seemed in this case to be organized in clusters rather than the banding that is more typical of occluded systems, such as in the 14 April 1980 case. The clusters persisted for the entire eight hours of satellite data. Because of the obscuring

cirrus cloudiness, the detection of the convective clusters with the digital IR data is more difficult in this case than in any of the others.

3.3 2 March 1980, Southeastern United States.

The storm over the Southeastern United States on 2 March 1980 is a classic example of Cape Hatteras development. At 0000 GMT 2 March, a stationary surface frontal system was located just off the coast of the U. S. Several waves of low pressure were situated along this front with the dominant center being located approximately 400nm south-southeast of Cape Hatteras. By 1200 GMT 2 March, only one center situated approximately 250nm southeast of the Cape remained. From this time through the end of the data period, 0000 GMT 3 March, the center intensified rapidly with a 16 mb central pressure drop occurring in the twelve hours ending 0000 GMT 3 March. A comparison of Figures 12b and 12c shows how slowly the cyclone center moved during the period of deepening.

A slight northwest-southeast orientation of the 500 mb short wave trough axis, acquired by 0000 GMT 3 March, suggests very intense PVA just east of the wave (Figure 13). The satellite imagery loops suggest that the PVA helped initiate the convective activity associated with this storm. As the PVA encountered the coastal frontal zone and a rather unstable airmass overlying the frontal inversion, rapid development of small convective clusters occurred. Near the termination of the satellite data period, 2100 GMT 2 March, an

extensive cirrus overcast developed over and to the east of the convective activity (Figure 16). The shield did not interfere with detection of the convection as in the previous case because of its advection downstream. Individual convective clusters persisted for several hours during the cyclone's propagation northeastward. The convective clusters appeared more vigorous in the imagery loops for this case than any of the other case studies.

3.4 31 January - 1 February 1981, Central United States.

The fourth and final case in the study was a rather uncommon one. The heaviest snowfall area was not associated with any organized storm center but rather with a poorly defined north-south oriented surface trough of low pressure. Development of a surface cyclone over southern Kansas was just beginning by 0000 GMT 1 February (Figure 17). A large anticyclone of Canadian origin had moved across the Great Lakes region during 30 January and was centered over Ohio by 1200 GMT 31 January. Associated with this event, troughing at the surface and aloft was occurring over the Rocky Mountains and western Great Plains. The southerly flow between the trough over the western Great Plains and the anticyclone over Ohio was quite intense and extended upward to at least 300 mb. Extensive warm advection was occurring through a deep layer of the atmosphere with a maximum located in the Nebraska-Kansas region.

The broad structure and northeast to southwest orientation of the 500 mb trough shown in Figure 18 does not suggest strong PVA over the central Plains. Hence, warm advection was apparently the primary

forcing for the upward motion and precipitation. The convective activity was embedded within the region of maximum warm advection. The convection increased in area and intensity during the afternoon hours apparently due to further destabilization above the 750 mb level through differential temperature advection (Figure 19). However, in this case all the bands were moving toward the northeast instead of spiraling around any circulation center. Cirrus cloudiness was present east of the convective activity; however, none was noted over the region of convection itself.

During the day, the system propagated eastward with little intensification. After 0000 GMT 1 February, the system intensified, accelerated toward the northeast, and attained a central surface pressure of 993 mb by 0000 GMT 2 February over the James Bay region of Canada.

4. DATA SAMPLE

The hourly surface synoptic reports and the digital IR brightness arrays used in this research were obtained through McIDAS. Data for the 14 April, 6 February and 2 March 1980 cases were retrieved from the system's extensive data archive containing the surface, upper air and satellite information received since approximately 1975. The data acquisition for the final case was completed in real time. In each instance, a listing of the surface observations for all stations reporting snowfall of any intensity was obtained each hour for a period of six to twelve hours (Figure 20a). Next, an hour by hour listing was produced for any station which reported moderate or heavy snowfall (S or S+) for at least one hour. An example for Raleigh-Durham, North Carolina is shown in Figure 20b.

The selection of location and time for which to obtain corresponding IR brightness arrays was based on the hourly variation of visibility for this subset of stations. A square cursor, defined to be 18 television pixels on a side, was centered on each of the desired stations in the hourly image. An array of visible and IR brightness values ranging between 0 and 255 were produced, an example of which is given in Figure 21a. Each array contains 324 data points, and each data point represents a 2nm x 2nm areal average brightness value. The total horizontal area encompassed by each array is approximately 1300 square nautical miles with small differences depending on the latitude and longitude of the centrally located station. From each array the

mean, median, mode and standard deviation of the brightness values were also obtained (Figure 21b). A complete listing of stations and hours for which arrays were produced in each case is shown in Tables 1 through 4.

STATION	HOUR (GMT)							
	16	17	18	19	20	21	22	23
Madison, WI			X	X	X	X		
Green Bay, WI			X	X	X			
Springfield, IL				X	X	X		
Manitowoc, WI				X	X			
Peoria, IL	X	X						
Ottumwa, IA	X	X	X	X	X	X		
Moline, IL	X	X	X	X	X	X		
Dubuque, IA	X	X	X	X				
Alpena, MI					X	X	X	X

Table 1: Stations and hours for which data arrays were produced for 14 April 1980 case.

STATION	HOUR (GMT)							
	14	15	16	17	18	19	20	21
Raleigh-Durham, NC	X	X			X	X	X	
Charlotte, NC	X	X	X	X				
Columbia, SC	X	X						
Lynchburg, VA		X	X	X	X	X	X	X
Roanoke, VA	X	X	X	X	X			
Danville, VA			X	X	X			
Greensboro, NC			X	X				
Dulles Int. Arpt.			X	X	X	X	X	
Washington Nat. Arpt.				X	X	X		
Martinsburg, WV			X	X	X	X	X	X
Baltimore, MD					X	X	X	X
Winston-Salem, NC		X	X	X				
Greenville, SC							X	X
Lewisburg, WV		X	X	X	X	X		
Fayetteville, NC			X	X	X			

Table 2: Stations and hours for which data arrays were produced for 6 February 1980 case.

STATIONS	HOURS (GMT)							
	14	15	16	17	18	19	20	21
Pt. Bragg, NC	X	X	X	N	X	X		
Myanna, MA	X	X	X	O	X	X		
Seymour, NC		X	X		X	X	X	X
Denville, VA	X	X	X	D	X	X	X	X
Elizabeth City, NC	X	X		A	X	X	X	
Pope AFB, NC		X	X	T	X			
Oceana NAS, VA		X	X	A	X			
Norfolk, VA	X	X	X		X			
Langley AFB, VA	X	X	X	A				
Anderson, SC			X	V	X			
Rocky-Mount, SC	X	X	X	A	X			
Hickory, NC	X	X	X	I	X	X	X	
Albany, GA	X	X	X	L	X			
Macon, GA	X	X	X	A	X	X		
Fayetteville, NC	X	X	X	L	X	X	X	
Raleigh-Durham, NC	X	X	X	A	X	X	X	
Atlanta, GA		X	X	B	X			
Winston-Salem, NC	X	X	X	L	X	X	X	
Greensboro, NC	X	X		E	X	X	X	
Nantucket, MA		X	X		X			

Table 3: Stations and hours for which data arrays were produced for 2 March 1980 case.

STATION	HOURS (GMT)							
	19	20	21	22	23	00	01	02
Norfolk, NE			X	X	N	X	X	X
Sidney, NE			X	X	O		X	X
Kansas City Int. Arpt.			X	X			X	X
Kansas City Muni. Arpt.			X	X	D		X	X
Hibbing, MN		X	X	X	A		X	X
Des Moines, IA		X	X		T		X	X
Topeka, KS		X	X	X	A			
St. Josephs, MO		X	X	X				
Mullen, NE	X	X			A			
Manhattan, KS	X	X			V			
Souix City, IA	X	X	X		A			
Beatrice, NE	X	X	X		I			
Lincoln, NE	X	X			L			
McCook, NE	X	X	X		A			
Omaha, NE	X	X	X	X	B			
Alliance, NE	X	X	X		L			
Ainsworth, NE	X	X	X		E			

Table 4: Stations and hours for which data arrays were produced for 31 January-1 February 1981 case.

5. PROCEDURES FOR CALCULATION OF PARAMETERS

In this study of the inference of convective precipitation intensity and intensity changes from geosynchronous satellite information, the report examines the following parameters:

- 1) deviation of the station point brightness value from the array areal average brightness, and
- 2) the Laplacian of the brightness field estimated by four different methods.

The following procedures were applied to each of the four cases investigated:

5.1 Selection of appropriate brightness arrays.

For a brightness array to be selected, (1) current hour snowfall intensity at the station about which the array is centered must differ from the intensity for either the previous or following hour and (2) standard deviation of the brightness values in the array must equal or exceed 2.0. Hence, only instances which displayed hourly intensity variations as well as variable cloud structure in the IR data were employed in the study. These restrictions reduced the number of arrays used for computations to approximately 200, from more than 300 arrays originally obtained from the four cases. A subset of 50 of these arrays which exhibited the most extreme variations in snowfall and cloud brightnesses (standard deviation >6.0) was considered separately, and a comparison of results is made between this subset and the larger array data base in the results.

5.2 Assignment of point brightness values.

Although McIDAS misalignment in point navigation routines is assumed to be no greater than 1nm for SMS-II data¹⁵ all brightness values used in calculations were obtained by averaging surrounding values to reduce navigation biases. The average point brightness was calculated from four surrounding points located equidistant from the central point. An example of the average point brightness calculation is presented in Figure 22, where the point brightness for the station at X is obtained by averaging the four surrounding values. The values on the array perimeter were not averaged.

5.3 Calculation of the five parameters for selected arrays.

In this study, the first parameter computed from each array was the deviation of the station brightness (DM) from the mean areal average brightness of the array. Positive values for DM imply that the cloud top above the station is colder and higher than the average cloud top in the array field. Similarly, negative values indicate a warmer and lower cloud top than the average value.

The two-dimensional Laplacian values of the brightness field centered on the station were the second parameters computed. The two-dimensional Laplacian operator ∇^2

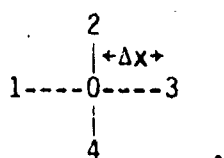
15. Griffeth, C. G., W. L. Woodley, P. G. Grube, D. W. Martin, J. Stout and D. N. Sikdar, 1978: Rain estimation from geosynchronous satellite imagery-visible and infrared studies. Mon. Wea. Rev., 106, 1153-1171.

$$\nabla^2 = \frac{\partial^2}{\partial x^2} + \frac{\partial^2}{\partial y^2}$$

in finite difference form is

$$\nabla_0^2 = \frac{(\)_1 + (\)_2 + (\)_3 + (\)_4 - 4(\)_0}{\Delta x^2} .$$

Here the subscripts indicate evaluation from scalar values, at the discrete points of the sketched grid array,



In this configuration to estimate the Laplacian, four of the points are distributed equidistant and orthogonal around a central point. The two-dimensional Laplacian of any scalar field is simply a measure of the rate of change of the horizontal gradient on a horizontal plane, and is used to locate both relative maxima and minima of values in the scalar field. Its sign is positive for relative minima and negative for relative maxima. When applied to an IR brightness field, the Laplacian effectively indicates the increased (decreased) vertical extent of a cloud top over the station, relative to the cloud tops at the perimeter points, associated with a brightness maxima (minima). This is accomplished through the cloud top height-temperature-IR brightness relationship previously discussed. As the "circularity" of these localized maxima and minima of brightness increase, so does the magnitude of the Laplacian. An example of the dependence of magnitude

upon "circularity" is shown in Figure 23.

The computed five point Laplacian (LAP1) values were highly dependent upon the orientation of the bright IR bands with respect to the orthogonal axes along which the discrete points are located. Figure 24 illustrates a situation where the five-point method results are misleading, due to dependence upon orientation. This dependency is a problem for the convective activity in the banded structure of cases one and four.

In an attempt to limit this problem a Laplacian with a nine-point structure (LAP2) based on a polar coordinate geometry was selected. Eight points are located equidistantly and symmetrically around a central point. Both the nine- and five-point structures behave similarly in terms of sign and magnitude characteristics. See Figure 25 for schematic representations of both Laplacian structures along with the equations used for calculations. The subscripted B values represent brightnesses at the respective numbered points used in the calculations.

The LAP1 and LAP2 were each calculated twice for all arrays; the ones with a grid interval of approximately 8 nm to be called the inner Laplacians (ILAP1 and ILAP2), and the others with an interval of 16 nm called the outer Laplacians (OLAP1 and OLAP2). Intercomparisons between Laplacians with different grid intervals were not made, and only the sign and relative magnitude of each type was considered. Hence, division by the square of the point separation (ΔX^2) was not necessary.

5.4 Parameter categorization.

The resultant values of the computation of the five parameters (DM, ILAP1, ILAP2, OLAP1, OLAP2), were compiled for individual stations and grouped by case number in tables similar to the example in Figure 26 for Madison, Wisconsin for the 14 April 1980 data, case number 1. The visibility (VIS) and weather (WX) data were obtained from the station listings described earlier. From the tabulated data, frequency distributions and mean values for the five parameters were generated and categorized according to snowfall intensity. Two categories were considered, light snow ($VIS > 0.7$ miles) and moderate or heavy snowfall ($VIS \leq 0.7$ miles). Potential relationships between the five parameters and the intensity of snowfall as it varied over space, from station to station, are scrutinized in the following section.

Another important consideration of this study was the temporal behavior of each parameter at a single location. Changes of each of the five parameters during one hour periods were calculated for all instances where snowfall intensity changed during the preceding hour (ΔDM , $\Delta ILAP1$, $\Delta ILAP2$, $\Delta OLAP1$, $\Delta OLAP2$). Here the resultant values are categorized under one of these headings:

- 1) positive intensity change (visibility reduction),
- 2) negative intensity change (visibility increase).

Hourly changes of the five parameters, as well as visibility, computed from the data in Figure 26 were compiled for each synoptic case in tables headed according to intensity change. Figure 27 shows an example of the tabulation format for intensity increases.

6. RESULTS

The results for estimates of precipitation intensity and intensity changes from GOES digital IR brightness for four cases of middle latitude convective activity imbedded in continuous stratiform precipitation are now presented. First, a comparison is made between means and frequency histograms of each parameter for the categories of spatially and temporally varying snowfall intensity, (S-) and (S,S+). The hourly changes in each parameter, means and frequency plots, are then computed and their ability to determine cases of intensity increases and decreases with time is tested. Next, an analysis of the most skillful indicators of snowfall intensity and intensity change is made. Finally, the above comparisons for intensity change are made for the special 50 array subset with standard deviation of brightness values equal to or exceeding 6.0.

6.1 Comparison of snowfall parameters with observed snowfall intensity.

Of the 210 IR brightness arrays meeting the mandatory requirements set forth earlier, 136 were centered on stations reporting light snowfall, while the remaining 74 arrays were for stations reporting moderate or heavy snowfall. Average values of all five parameters and visibility were calculated for these two intensity categories, and the results are presented in Table 5. All of the tests are based on the hypothesis that, for convection embedded in regions of continuous snow, a station reporting a heavy snowfall intensity would have a cloud top

	<u>S-</u>	<u>S.S+</u>
AVERAGE VISIBILITY (\overline{VIS})	1.7	0.5
AVERAGE STATION DEVIATION FROM MEAN (\overline{DM})	-0.1	-0.6
AVERAGE INNER 5 POINT LAPLACIAN ($\overline{ILAP1}$)	1.2	-0.1
AVERAGE OUTER 5 POINT LAPLACIAN ($\overline{OLAP1}$)	0.6	0.3
AVERAGE INNER 9 POINT LAPLACIAN ($\overline{ILAP2}$)	1.6	1.5
AVERAGE OUTER 9 POINT LAPLACIAN ($\overline{OLAP2}$)	1.1	2.9

Table 5: Average values of all parameters and visibility for each snowfall intensity category.

	<u>S-</u>	<u>S.S+</u>
\overline{DM}	-	+
$\overline{ILAP1}$	+	-
$\overline{OLAP1}$	+	-
$\overline{ILAP2}$	+	-
$\overline{OLAP2}$	+	-

Table 6: Hypothesized sign distribution of parameter averages for each snowfall intensity category.

of much larger vertical extent located above it, relative to nearby areas. Thus, one would expect a relative maximum of IR brightness in the array at the station location. The distribution of the signs of the computed parameters shown in Table 6 idealized by this hypothesis is likely valid for the cases examined when the areal extent of relative maxima or minima of intensity and brightness are encompassed within the 36 nm x 36 nm area of the array.

Mean values of all the parameters display the expected sign for the light snow category. However, the sign expectations for the heavier (S,S+) occurrences were only satisfied for OLAP1, and even then its value is only slightly negative. The values in Table 5 suggest that an occurrence of light snowfall with an average visibility of 1.7 miles is indeed associated with an IR brightness minimum relative to nearby areas, but a similar interpretation cannot be made for the heavier intensity occurrences from the four cases.

Mean parameter values for each of the synoptic cases individually are shown in Table 7. Recall that in cases one and four the imbedded convection displayed a banded structure, while in cases two and three the convection is cellular. The computational results in Table 7 for the nine point Laplacian averages, both small and large scale, for cases one and four resulted in the hypothesized sign distribution. Such was not the situation for cases two and three involving primarily cellular convection (Table 7).

The frequency histograms for all five parameters in Figures 28 through 30 exhibit large variance of values for both intensity cate-

CASE NUMBER	<u>S-</u>				<u>S.S+</u>			
	1	2	3	4	1	2	3	4
NUMBER OF OCCURRENCES	19	44	46	27	14	4	37	19
DM	-2.2	0.7	-0.3	0.2	-0.5	-2.0	-0.1	-1.6
ILAP1	8.7	-0.7	0.3	0.7	1.5	5.0	-0.7	-1.4
OLAP1	5.9	-2.5	2.7	-1.6	3.0	15.5	2.0	-6.4
ILAP2	7.4	-0.4	0.7	0.5	-3.5	3.5	1.7	-3.1
OLAP2	8.2	-1.6	0.6	1.4	-0.4	7.0	3.4	-2.1

Table 7: Parameter averages and number of occurrences for each snowfall intensity category for individual synoptic cases.

	<u>S-</u>	<u>S.S+</u>
DM	5.1	4.2
ILAP1	21.3	10.1
OLAP1	30.1	20.2
ILAP2	15.2	12.8
OLAP2	20.4	27.3

Table 8: Standard deviations of parameter values for each intensity category.

gories. Standard deviations for each are shown in Table 8. The large variances, coupled with the near zero values for all parameter averages, imply that within the array the overall relationship between the means of the parameter and snowfall intensity is difficult to determine. However, a relationship is seen between the nine-point Laplacian averages and intensity for cases of banded convection.

One subtle difference between the intensity categories for each parameter is in the skewness of the frequency distributions. Positive skewness implies a tendency for observations to cluster in the upper half of the range of values, while negative skewness means that more observations are found in the lower half. Figures 28 through 30 present frequency histograms of the DM, ILAP1, OLAP1, ILAP2, OLAP2 values for both intensity categories. Note that distribution of parameters within each frequency interval is given by $f_1 < f < f_1 + \Delta f$.

Little skewness is evident in the distribution of station brightness deviation (DM) from the array mean, but rather a flat Gaussian type distribution with a maximum frequency near zero is found.

The distributions for the two outer Laplacians (OLAP1 and OLAP2) display slight positive skewness for light snowfall occurrences, and a negative skewness for the heavier intensities. This suggests a relative brightness maximum is associated with the majority of heavy (S,S+) occurrences, and a relative minimum for the light intensities. However, both inner Laplacian distributions have a maximum frequency in the interval immediately above zero for the heavier intensities

suggesting relative minima of brightness are usually associated with the heavy snowfall occurrences, a result opposite to the hypothesized distribution.

In summary, the OLAP1 and OLAP2 distributions are skewed somewhat in the expected directions, and of those two, the nine-point structure (OLAP2) seems to produce the most favorable results when compared to the hypothesized brightness-intensity relationship presented earlier. However, a definite inference of snowfall intensity, based solely upon the five parameters just examined, does not seem promising.

One possible reason for the failure of these methods to adequately detect the regions of enhanced snowfall intensity is a horizontal displacement between the heavy snowfall area at the surface and the convective clouds producing the heavy snow. This displacement may occur with strong wind shear, in both direction and speed, which cause the snow to blow a considerable horizontal distance from its point of formation in the clouds until it reaches the earth's surface. With a 4 km level of origin and a 1 m/s fall velocity¹⁶, a mean wind of 4 m/sec relative to the cloud of origin and the earth's surface will produce a typical displacement of 12-16 km. The mean wind in this case is defined to be the average wind between the earth's surface and the level of origin. For a linear increase with height, this relative mean wind of 4 m/sec corresponds to a wind difference of 8 m/sec from the earth's surface to the level of origin. Strong wind shear was present

16. Rogers, R. R., 1979: A Short Course in Cloud Physics. Pergamon International Library, 235 pp.

in all cases examined. This effect is likely enhanced for very narrow bands or clusters of enhanced intensity.

Figure 31 shows the Madison, Wisconsin centered IR brightness from Case 1 arrays for 1900, 2000 and 2100 GMT, contoured every 10 units, superimposed on the concurrent WSR57 radar depictions from Neenah, Wisconsin. The shaded areas represent radar returns of level two or greater (scaled from 1 to 6). Note the alignment of the heavier precipitation areas, inside the array boundaries, with the largest brightness values. At 1900 GMT and again at 2000 GMT, MSN reported 0.5 mile visibility in moderate snowfall, even though the orientation of brightness maxima within the array would imply a relative minimum of brightness directly over the station itself. The largest values of both IR brightness and radar return were located to the east-northeast of MSN. Wind flow at all levels up to and including 300 mb was from the northeast at 1200 GMT with the maximum speed of 26 m/sec at 850 mb. This suggests that the snow did indeed blow southwestward as it fell, displacing the region of heavy snowfall at the surface from the clouds which produced it.

The problem of downwind displacement of heavy snow due to wind shear was not anticipated in the initiation of this research. However, during the conduct of the research, facets of this problem became evident. The more detailed analysis including radar information from case 1 suggests that displacement of the snow between the convective clouds of origin and the point of deposition is a likely reason for the

lack of success in the statistical analysis. It seems that the displacement problem could be reduced by using a technique which centers the arrays of long lived, easily tracked brightness maxima and minima. A comparison of parameter values for those stations reporting variable snowfall intensities near and downwind of the array center could be conducted. A comparison of results from such a study with the results of this research would be most informative.

6.2 Comparison of snowfall parameter changes with observed hourly snowfall intensity changes.

During the four cases a total of 55 intensity increases and 62 decreases occurred. In these events hourly changes for each of the five parameters and visibility were computed from the data and tabulated as described earlier (Figure 27). The mean values are given in Table 9.

Just as a relative maximum in the IR brightness field over stations reporting moderate to heavy snowfall would be expected, the hypothesis anticipates that an increase in relative brightness would ideally be found over stations experiencing an increase in intensity. Likewise, a decrease in relative brightness values would be found over stations reporting decreases in snowfall intensity. If this were indeed the case, the sign distribution seen in Table 10 would be expected for the parameter change averages for each intensity change category. This expected distribution was, in fact, realized for all but two of the ten average parameter change-intensity change

	<u>INCREASE</u>	<u>DECREASE</u>
AVERAGE HOURLY VISIBILITY CHANGE ($\overline{\Delta VIS}$)	-0.4	0.7
AVERAGE HOURLY CHANGE IN DM ($\overline{\Delta DM}$)	0.0	-0.4
AVERAGE HOURLY CHANGE IN ILAP1 ($\overline{\Delta ILAP1}$)	-1.9	1.6
AVERAGE HOURLY CHANGE IN OLAP1 ($\overline{\Delta OLAP1}$)	1.0	1.3
AVERAGE HOURLY CHANGE IN ILAP2 ($\overline{\Delta ILAP2}$)	-4.6	1.8
AVERAGE HOURLY CHANGE IN OLAP2 ($\overline{\Delta OLAP2}$)	-5.2	5.6

Table 9: Average hourly changes in all parameters for each intensity change category.

	<u>INCREASE</u>	<u>DECREASE</u>
$\overline{\Delta VIS}$	+	-
$\overline{\Delta DM}$	-	+
$\overline{\Delta ILAP1}$	-	+
$\overline{\Delta OLAP1}$	-	+
$\overline{\Delta ILAP2}$	-	+
$\overline{\Delta OLAP2}$	-	+

Table 10: Hypothesized sign distribution of average hourly parameter changes for each intensity change category.

combinations, $\overline{\Delta DM}$ and $\overline{\Delta ILAP1}$. Magnitudes of the average changes, of all parameters except for $\overline{\Delta DM}$, were larger than the corresponding magnitudes of the instantaneous values for each hour seen in Table 5 earlier.

Figures 32 through 34 contain the frequency histograms of parameter changes for both intensity change categories. The ΔDM and $\Delta ILAP1$ distributions show very little, if any, skewness, with maximum frequencies very near zero. Of the remaining distributions, the nine-point Laplacian changes show the largest negative shift in their distributions for intensity increases, and slight positive shifts for decreases in intensity. In particular, a considerable negative displacement of the frequency maximum is noted for intensity increases in the distributions of $\Delta ILAP2$ and $\Delta OLAP2$ (Figure 34). This accurately represents the hypothesized distributions, and suggests that snowfall intensity increases might well be indicated by hourly decreases in values of the nine point Laplacians. In general, the skewness displayed by the parameter change-intensity change distributions is larger than that for the parameter value-intensity histograms shown earlier. Also, when present, the skewness is in the expected direction.

6.3 Determination of most skillful indicators for intensity and intensity change.

The ability of the five parameters and their changes to discriminate between each intensity and intensity change category was

tested through computation of a frequency difference for each interval. This was accomplished by subtracting the (S,S+) frequency value from the corresponding (S-) frequency value in a given interval for a particular parameter. The same procedures were applied to the hourly change histograms, with the intensity increase frequency in an interval subtracted from the corresponding intensity decrease frequency for each parameter change.

Based upon the idealized relationships of IR brightness to intensity and brightness change to intensity change discussed earlier, an (S-) bias in the difference of the frequencies is expected for DM values less than zero and a (S,S+) bias in the difference for positive DM values. Similarly, the frequency difference of Laplacian values should favor (S-) in positive intervals and (S,S+) in negative intervals. The frequency difference computations are a measure of histogram overlap between the two intensity and intensity change categories considered for each parameter. A perfect overlap (two identical distributions) would have a zero difference for each frequency interval, would be indicative of random distributions for the snowfall parameter and would imply no capability to discriminate snowfall intensity at the earth's surface. Conversely, no overlap at all (two completely dissimilar distributions) would indicate certainty in discriminating snowfall intensity or change.

The frequency difference distributions for each parameter are shown in Figures 35 and 36. In these figures, the subtotal for positive and negative intervals of each parameter and parameter change

are plotted in the appropriate quadrant of each diagram. In Figure 35 for example, the difference frequencies for DM show a subtotal for positive intervals of one percent in favor of (S-) occurrences, while the subtotal frequency difference for the negative intervals favors (S,S+) occurrences by 5 per cent. These subtotals are extremely small for both intervals. In fact, the distributions for (S-) and (S,S+) observations are nearly perfectly overlapped; hence, inference of intensity using DM as an indicator was not justified. In the four cases examined, any randomly chosen DM value for the array centered station would have a nearly equal likelihood of being associated with an (S-) or an (S,S+) observation.

Only the frequency differences for OLAP1 and OLAP2 display the expected distribution, with the largest sum of differences being 22 for OLAP1. Based upon the data from the synoptic cases chosen, these results indicate that if negative values of OLAP1 were obtained from the array data base, only 10 per cent would be uniquely associated with (S,S+) observations while 90 per cent would have been associated with either (S-) or (S,S+) occurrences. Similarly, only 12 percent of the positive values obtained would be uniquely associated with (S-) occurrences and 88 percent could be associated with either intensity. Thus, an accurate determination of snowfall intensity would have been possible for only 11 percent of the total OLAP1 values obtained under the assumption of an equal probability for positive and negative values in the sample. Since OLAP appears to be the most skillful intensity indicator of the five parameters considered, it was concluded that

inference of snowfall intensity using the methods of this study where the centroid of the Laplacian snowfall parameter is located with the observing station does not yield reasonable accuracy. However, the colocation of areas of radar return and brightness values in the case 1 suggests that discrimination would be sharpened if allowances were made for the displacement of falling snow between level of origin and surface deposition due to wind shear.

The distributions of frequency differences for all parameter changes are presented in Figures 37 and 38. $\Delta ILAP2$ and $\Delta OLAP2$ have the largest subtotal as well as total frequency differences. Correct determination of intensity change was possible for 27 percent and 29 percent of the $\Delta ILAP2$ and $\Delta OLAP2$ samples, respectively. This is a significant percentage of intensity changes. Further work in development and modification of the methods used in this study in conjunction with snowfall displacement due to wind shear should be undertaken to improve the reliability of intensity change inferences.

6.4 Determining intensity change for the 50 array subset (standard deviation of brightness in the array of at least 6.0).

The selection of a restricted data subset with a standard deviation of at least 6.0 for array values means that only those arrays with extreme variations of IR brightness are considered. The magnitudes of the parameter changes for this subset (Table 11) are consequently larger, than are the average magnitudes for parameter

	<u>INCREASE</u>	<u>DECREASE</u>
<u>ΔDM</u>	0.9	-0.2
<u>$\Delta I LAP1$</u>	-7.9	1.7
<u>$\Delta O LAP1$</u>	-7.1	1.2
<u>$\Delta I LAP2$</u>	-3.2	4.4
<u>$\Delta O LAP2$</u>	-9.4	4.3

Table 11: Average hourly parameter changes for each intensity change category, for the special 50 array subset (standard deviation of brightness values >6.0).

changes for the entire sample. The total number of intensity changes in each category with 31 increases and 30 decreases is approximately half that for the entire array data set.

Within this subset, all parameter change averages display the expected sign (Table 10). The frequency histograms also exhibit more displacement between maximum frequency intervals for cases of intensity increase versus decrease (Figures 39 through 41). However, the distribution overlap is also greater, thus the reliability of intensity change determination inferred from the frequency difference diagrams, of Figures 42 and 43, is not increased. The most skillful indicator of intensity change for the 50 array subset intensity change is $\Delta ILAP2$ with a total frequency difference of 57, less than the most skillful indicator of intensity change for the entire array set.

In this array subset, large standard deviations of brightness values of small scale horizontal variations in cloud structure are likely present. Thus, the ability of the Laplacian to accurately resolve smaller scale maxima and minima in the brightness fields may be decreased. In an extreme case, possibly several maxima and/or minima may exist within the finite grid area used for the Laplacian estimates within a given array. Under these circumstances, the discrete estimates of the Laplacians of the brightness data may indicate erroneous values. To analyze this problem, higher resolution satellite imagery than that produced for this study must be used. Also, the problem of displacement of the snow by wind shear may be compounded for very small scale convection.

7. CONCLUSIONS

This report presents a pilot study designed to develop techniques applicable to middle latitudes for inferring precipitation intensity and intensity changes in cases of continuous precipitation from GOES IR brightness data. Although the results obtained in this study involved precipitation only in the form of snow, they likely also are applicable to studies of intensity and intensity change of showers embedded in continuous rain. Snow was chosen because of the close relation between intensity and horizontal surface visibility.

The satellite and conventional data for use in the study were obtained through McIDAS at the University of Wisconsin-Madison. A data base consisting of hourly digital IR brightness value arrays that were centered on stations with large temporal variations in snowfall intensity was formed. Four snowstorm cases were selected from a total of fifteen cases examined during the winters of 1979-80 and 1980-81. Selection was based upon the criteria of variability of snowfall intensity and cloud structure during the storms. A total of 210 arrays were used, each having a required standard deviation in brightness values of at least 2.0.

Five numerical parameters were then estimated from each array of digital IR brightness values. They included deviation of station brightness (DM) from the average array brightness, two five-point station centered Laplacian of the brightness field (one with a 16 nm horizontal scale (ILAP1) and the other with a 32 nm horizontal scale

(OLAP2)) and two nine-point station-centered Laplacians of the brightness values, with horizontal scales the same as the five-point structure.

Mean values and interval frequency histograms were constructed for each of the five parameters according to observed snowfall intensity at the array centered station. Results based upon the distributions of the means and frequencies showed that for the most skillful indicator of intensity (OLAP1), positive determination of precipitation intensity at a locale was possible only approximately 10 per cent of the time. The hourly changes in the five parameters was examined in a similar manner for cases of intensity (visibility) change from hour to hour. All parameter changes displayed distributions expected from an idealized relationship of cloud structure to intensity. The most skillful indicator of intensity changes (Δ OLAP2) was able to correctly infer the change nearly 30 per cent of the time.

Based upon these results, inference of intensity for cases of continuous precipitation in middle latitudes does not seem feasible if only relative variations in the IR brightness values distributed over a given location are considered. Intensity change, however, apparently can be inferred a significant percentage of the time, and study aimed at further developing these techniques seems appropriate.

Several problems with the methods used were realized during the course of the study. The primary problem seemed to be horizontal displacement of snow during its fall from its level of origin to its

point of deposition; a problem that could not be compensated for in this research. The observed intensity at the surface and the location of the clouds producing the heavier precipitation in these cases of strong wind shear were not colocated. In a preliminary comparison, using Case 1 data, maxima fields of the radar return and satellite IR brightness were co-located 10 to 15 miles northeast of the surface points of maximum snowfall. If the model had included provisions for the drift of falling snow due to wind shear, the evidence suggests that the discrimination would have been increased substantially. In future studies that address the nowcasting problem of mesoscale precipitation in the form of snow, a degree of freedom should be included to account for the displacement of falling snow of convective origin. This problem would undoubtedly be much less prominent for rainfall cases.

A technique which centers the arrays on easily tracked brightness maxima and minima is suggested. The arrays would be moved to coincide with positions of the maxima or minima and the discrimination ability of parameter values and parameter changes would be tested for stations located near and downwind from the array centers.

Another problem was the inability of the conventional five-point Laplacian structure to adequately describe variations in the IR brightness field for banded convection. This problem was reduced by using a nine-point Laplacian structure (eight perimeter points and one central point).

The same methods to estimate snowfall intensity change were applied to a special array subset of fifty occurrences of increased

variability of the brightness values within the arrays. The reliability of estimation of snowfall intensity changes from the five parameter was not increased in this subset.

In retrospect, the use of only snowstorm cases in this research was likely a limitation in the inference of precipitation intensity from satellite information. Variations in observed intensity of snowfall are possibly not as well related to parameters used in this study as the relation might be with rainfall. Rainshowers in warmer seasons are associated with a warmer and somewhat less stable troposphere. Thus, depth and organization of the convective systems of rainshowers is likely more pronounced. Consequently, parameters utilizing cloud top temperatures to estimate showery precipitation should discriminate better in conditions of rainshowers than snowshowers. In addition, the problem of displacement would be reduced due to the increased fall velocity of raindrops over snowflakes. However, because of these different fall rates, the analysis to infer precipitation intensity and/or intensity changes should be completed separately for snow and rain, due to the ambiguity of larger displacement for snow in a wind-sheared atmosphere.

BIBLIOGRAPHY

- Adler, R. F., and D. D. Fenn, 1978: Thunderstorm intensity as determined from satellite data. J. Appl. Meteor., 18, 502-517.
- Brandli, H. W., 1976: Satellite Meteorology, Air Weather Service Tech. Rep., AWS-TR-76-264, Hq Air Weather Service, Scott AFB, IL., 188 pp.
- Griffeth, C. G., W. L. Woodley, P. G. Grube, D. W. Martin, J. Stout and D. N. Sikdar, 1978: Rain estimation from geosynchronous satellite imagery-visible and infrared studies. Mon. Wea. Rev., 106, 1153-1171.
- Hobbs, P. V., and J. D. Locatelli, 1978: Rainbands, precipitation cores and generating cells in a cyclonic storm. J. Atmos. Sci., 35, 230-241.
- Houze, R. A., Jr., P. V. Hobbs, K. R. Biswas and W. M. Davis, 1976: Mesoscale rainbands in extratropical cyclones. Mon. Wea. Rev., 104, 868-878.
- Johnson, G. L., and D. Suchman, 1980: Intercomparisons of SMS wind sets: a study using rapid scan imagery. Mon. Wea. Rev., 108, 1672-1688.
- Rogers, R. R., 1979: A Short Course in Cloud Physics. Pergamon International Library, 235 pp.
- Schofield, R. A., and V. J. Oliver, 1977: A scheme for estimating convective rainfall from satellite imagery. NESS Tech. Memo. 86, NOAA, 47 pp.
- Sikdar, D. N., 1971: ATS-3 observed cloud brightness field related to a meso-to-synoptic scale rainfall pattern. Tellus, 24, 400-412.
- Smith, W. L., V. E. Suomi, W. P. Menzel, H. M. Woolf, L. A. Sromovsky, H. E. Revercomb, C. M. Hayden, D. N. Erickson and F. R. Mosher, 1981: First sounding results from VAS-D. Bull. Amer. Meteor. Soc., 62, 232-236.
- Stout, J., D. Martin and D. N. Sikdar, 1979: Estimating rain with geosynchronous satellite images. Mon. Wea. Rev., 107, 585-598.
- Wash, C. H., J. Stremikis and D. R. Johnson, 1979: Objective forecasts of subsynoptic convective areas using interactive computer systems. AMS Preprint Volume, 11th Conference on Severe Local Storms, 2-5 October 1979.
- Wylie, D. P., 1979: An application of a geostationary satellite rain estimation technique to an extratropical area. J. Appl. Meteor., 18, 1640-1648.

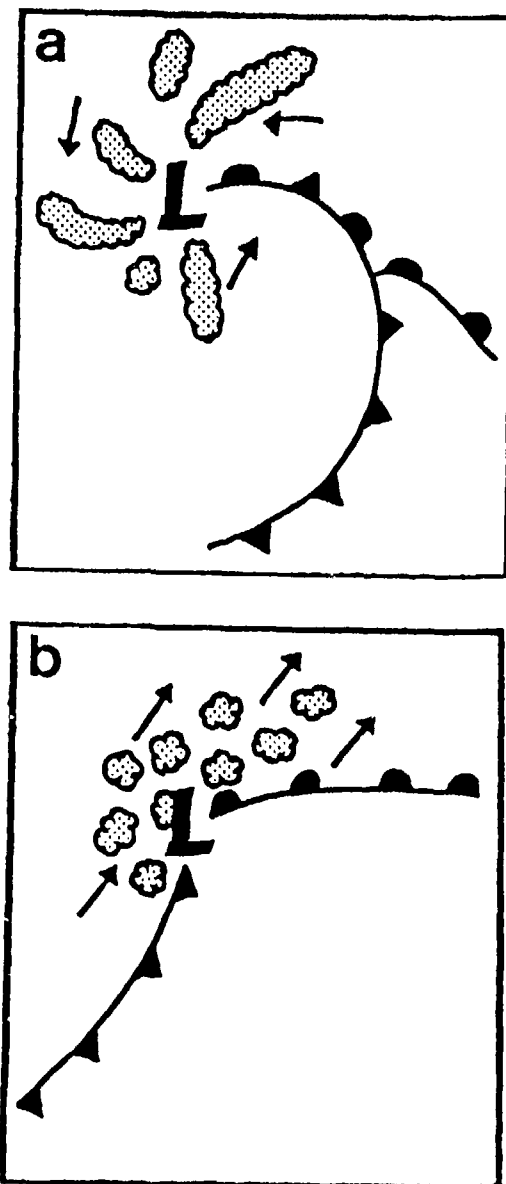


Figure 1: Typical distributions of mesoscale convective bands associated with (a) an occluded cyclone and (b) a developing cyclone. Arrows indicate movement of convective activity.

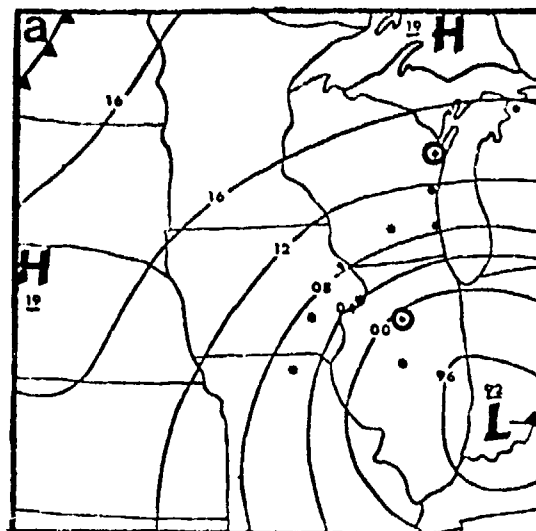
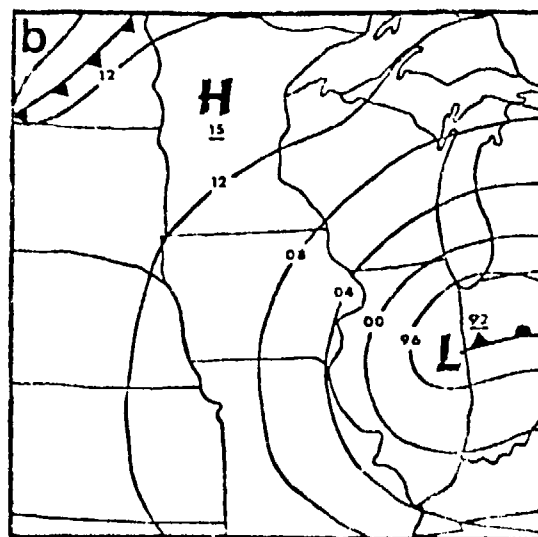
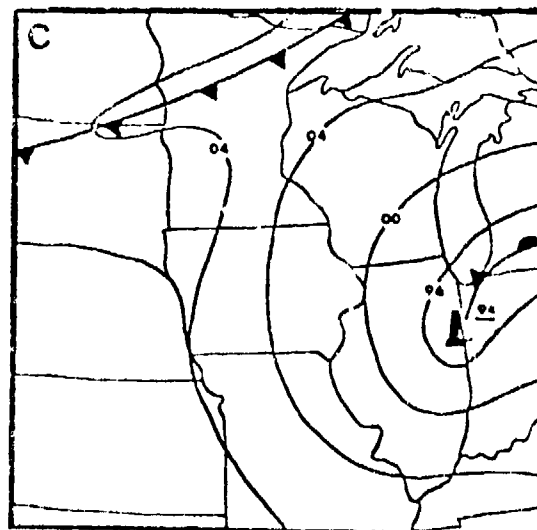


Figure 2: NMC surface analyses for (a) 1200 GMT 14 April 1980, (b) 1800 GMT 14 April 1980 and (c) 0000 GMT 15 April 1980. Stars in (a) locate stations on which brightness arrays were centered, circles indicate sounding stations used.



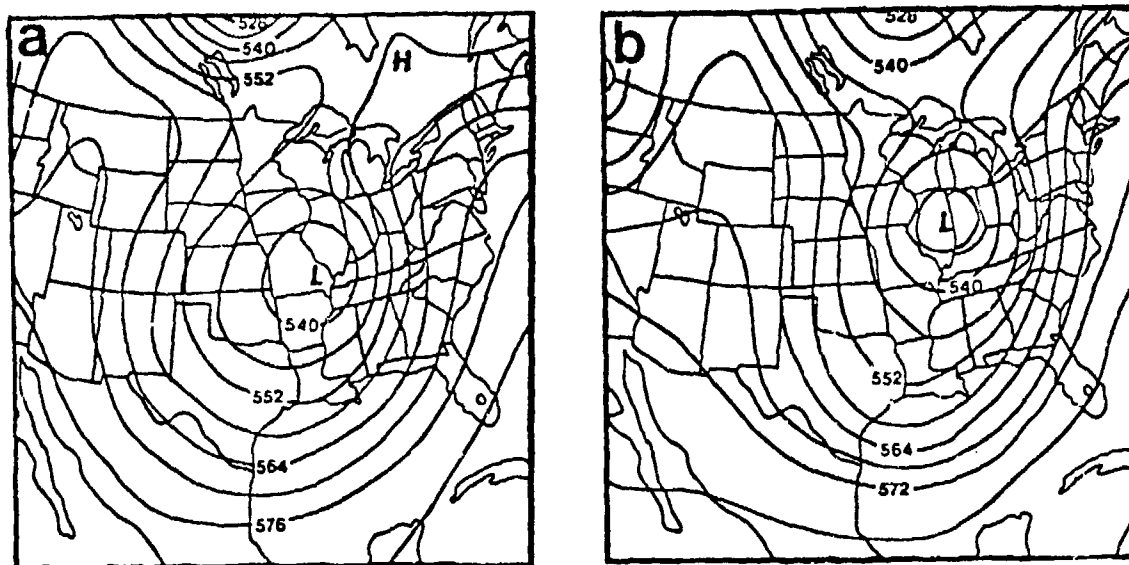


Figure 3: NMC 500 mb geopotential analyses (heights in decameters) for (a) 1200 GMT 14 April 1980 and (b) 0000 GMT 15 April 1980.

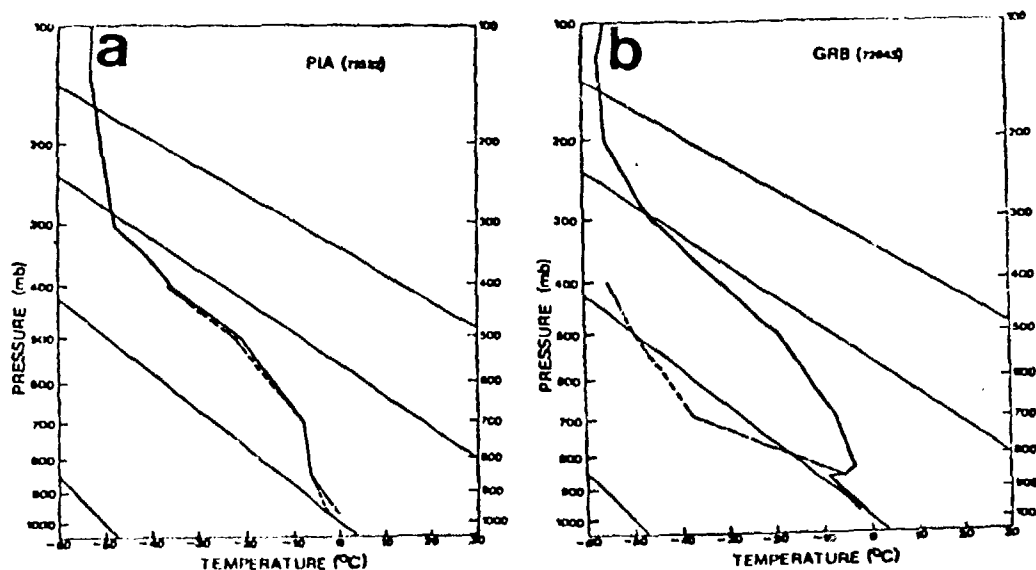
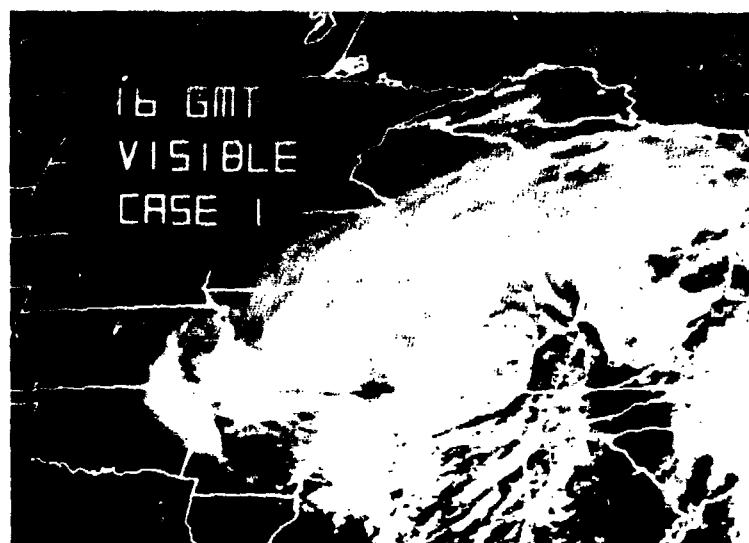


Figure 4: Vertical distributions of temperature (solid lines) and dewpoint (dashed lines) for (a) Peoria, Illinois and (b) Green Bay, Wisconsin, 1200 GMT 14 April 1980.

a)

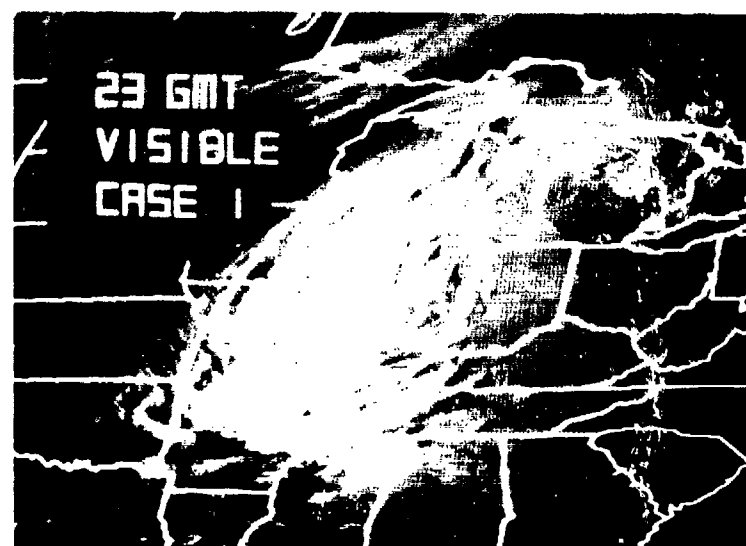


b)



Figure 5: SMS-II satellite imagery; (a) visible and (b) infrared, 1600 GMT 14 April 1980.

a)



b)



Figure 6: Same as Figure 5 except for 2300 GMT 14 April 1980.

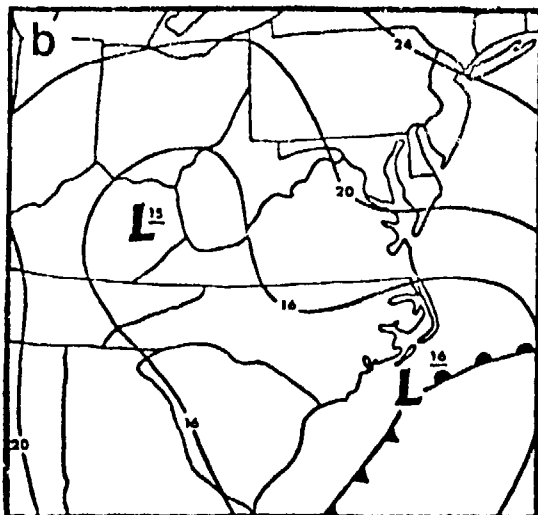
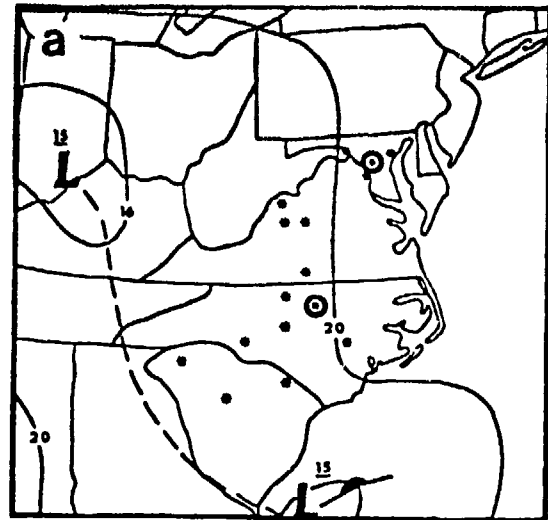
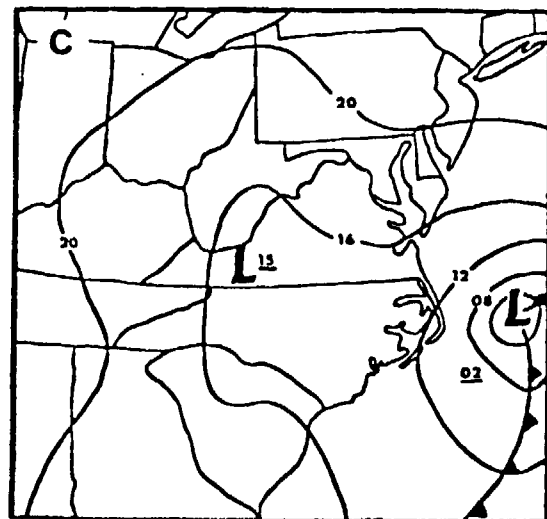


Figure 7: Same as Figure 2 except for (a) 1200 GMT 6 February 1980, (b) 1800 GMT 6 February 1980 and (c) 0000 GMT 7 February 1980.



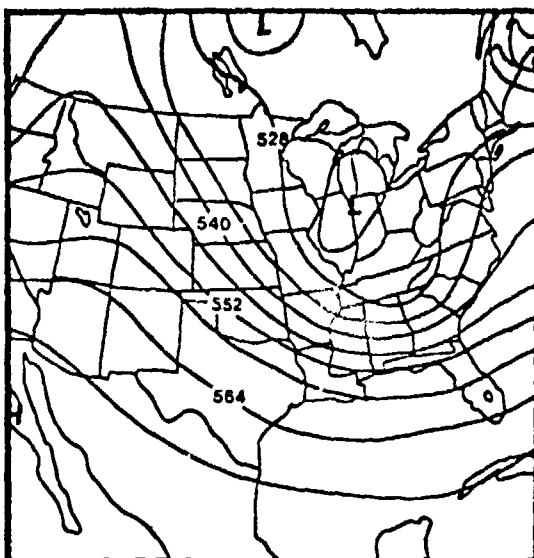


Figure 8: Same as Figure 3 except for 1200 GMT 6 February 1980.

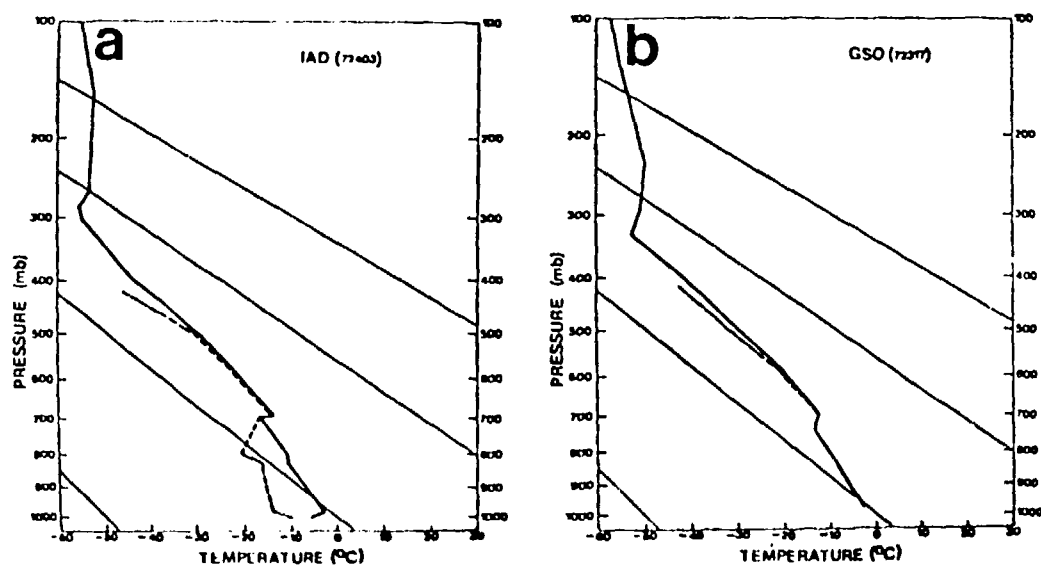
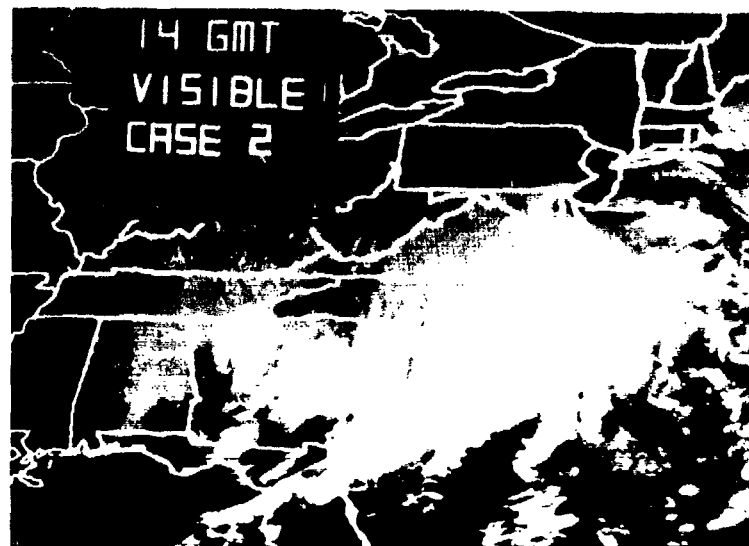


Figure 9: Same as Figure 4 except for (a) Dulles International Airport, Maryland and (b) Greensboro, North Carolina, 1200 GMT 6 February 1980.

a)



b)

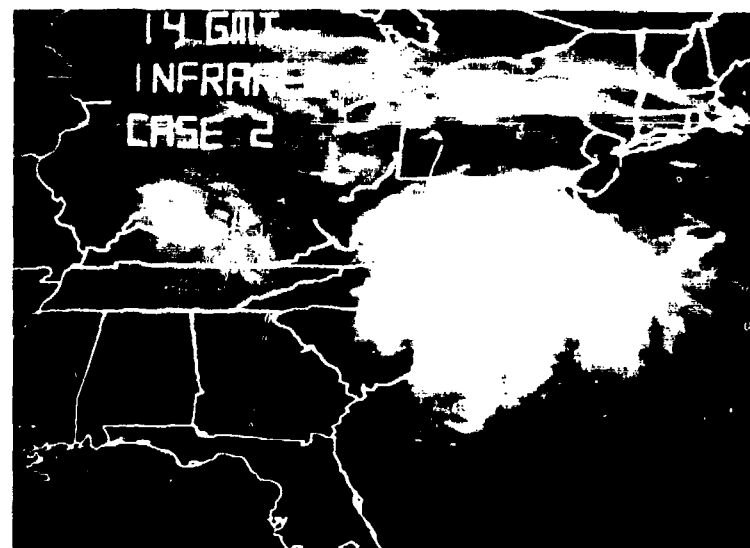
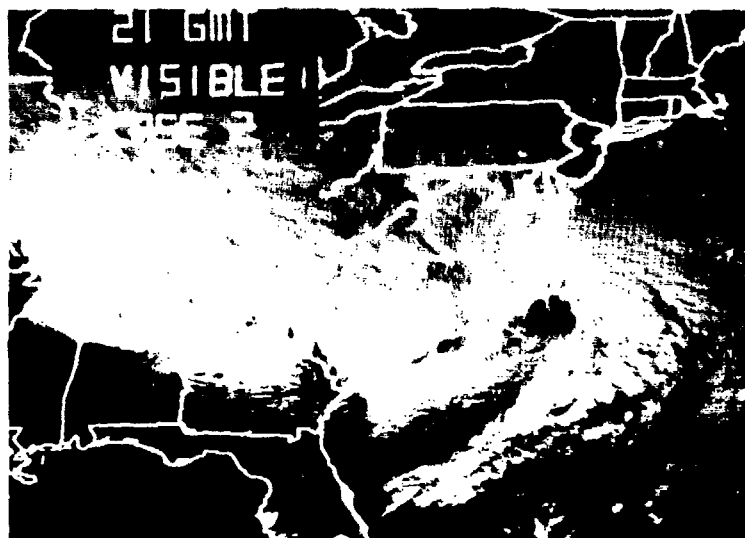


Figure 10: Same as Figure 5 except for 1400 GMT 6 February 1980.

a)



b)



Figure 11: Same as Figure 5 except for 2100 GMT 6 February 1980.

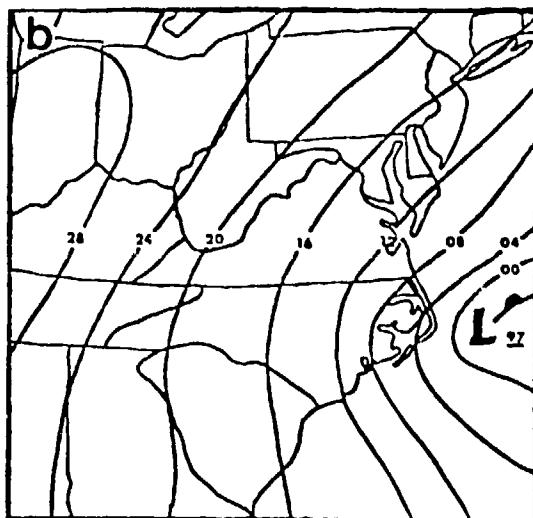
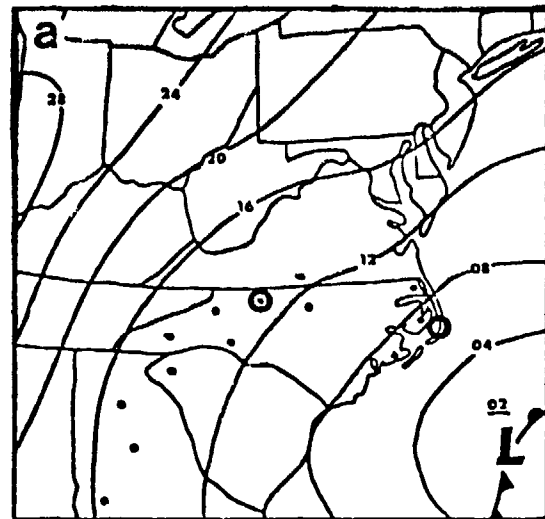
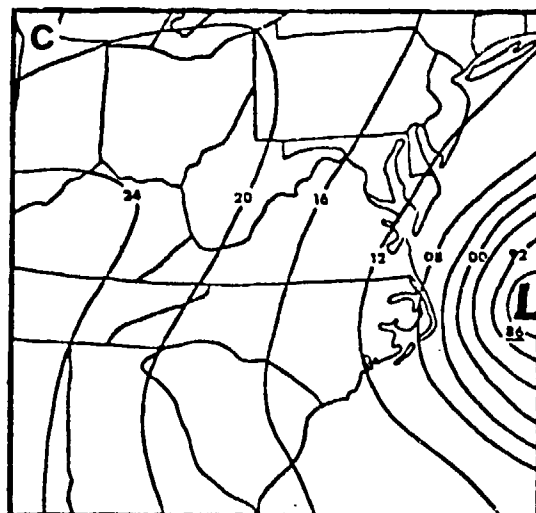


Figure 12: Same as Figure 2 except for (a) 1200 GMT 2 March 1980, (b) 1800 GMT 2 March 1980 and (c) 0000 GMT 3 March 1980.



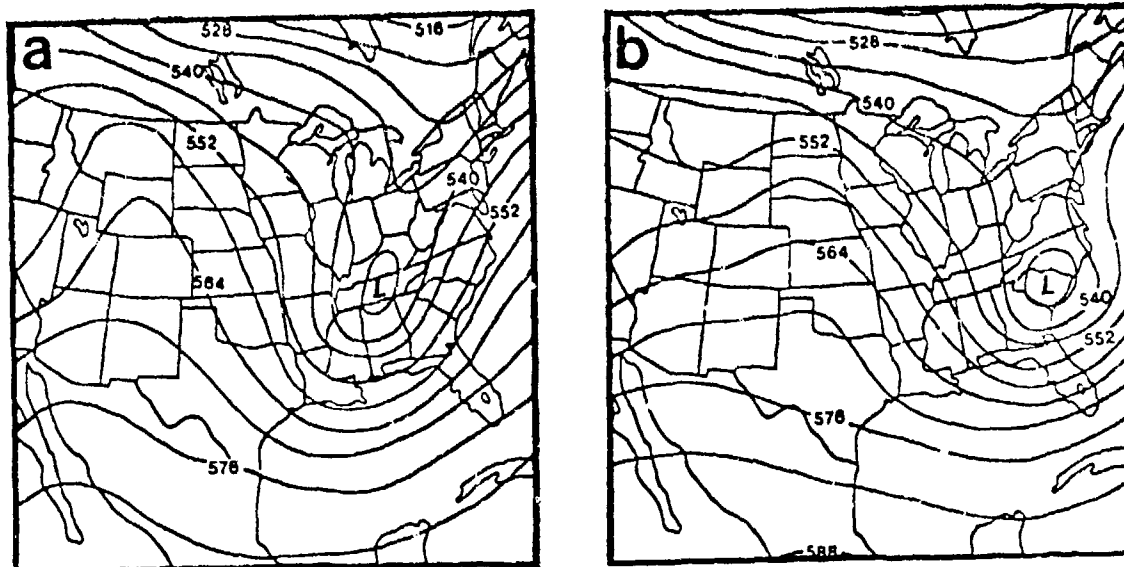


Figure 13: Same as Figure 3 except for (a) 1200 GMT 2 March 1980 and (b) 0000 GMT 3 March 1980.

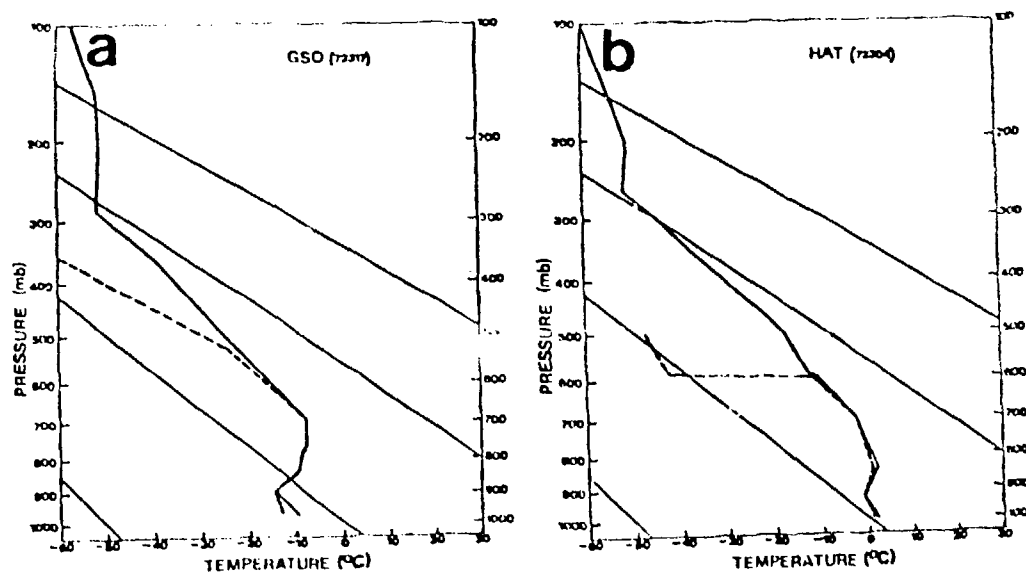
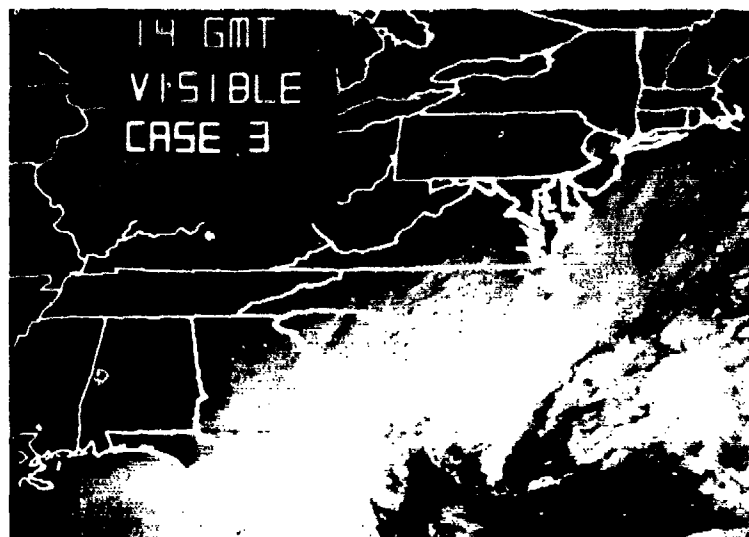


Figure 14: Same as Figure 4 except for (a) Greensboro, North Carolina and (b) Cape Hatteras, North Carolina, 1200 GMT 2 March 1980.

a)



b)

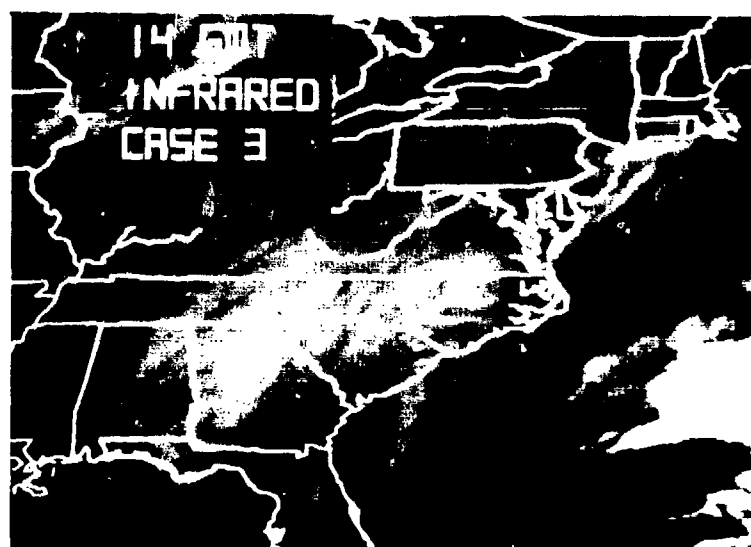
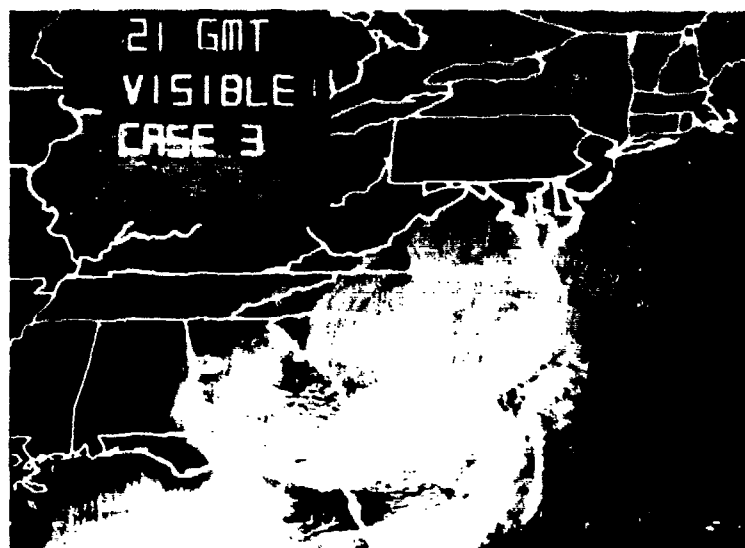


Figure 15: Same as Figure 5 except for 1400 GMT 2 March 1980.

a)



b)

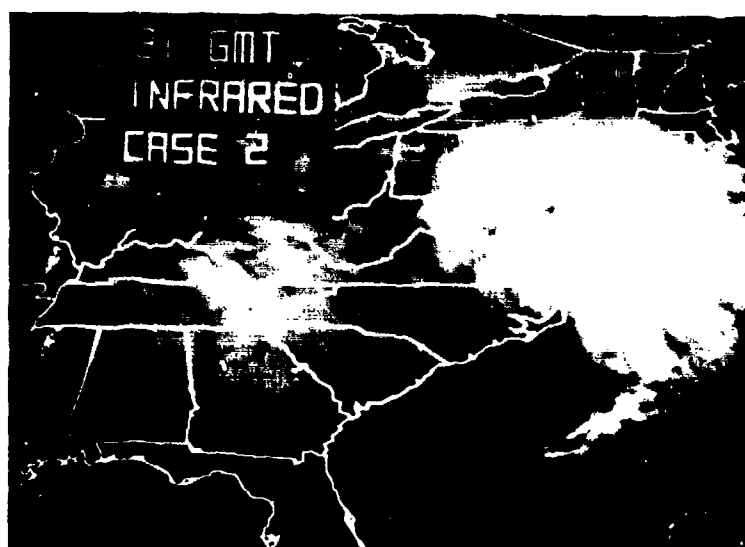


Figure 16: Same as Figure 5 except for 2100 GMT 2 March 1980.

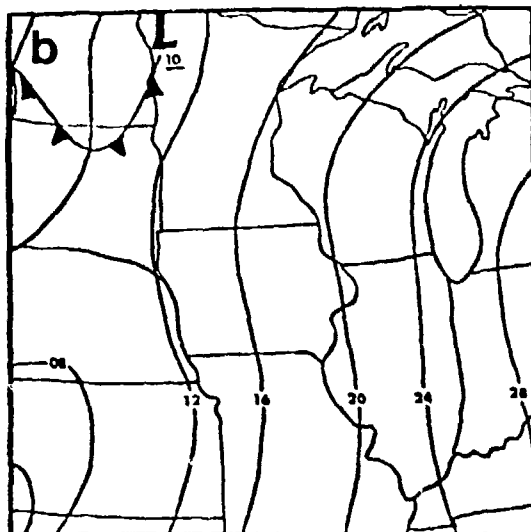
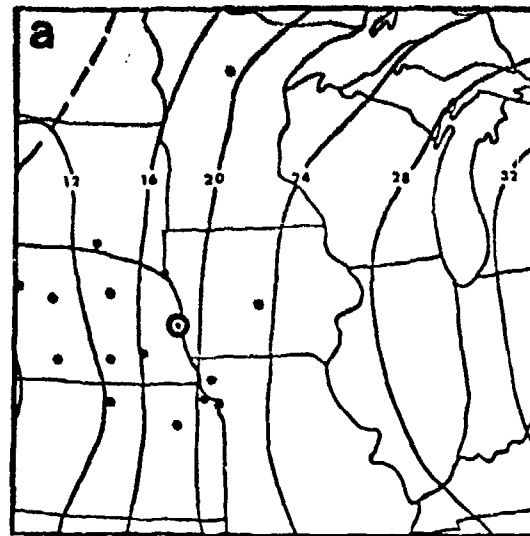
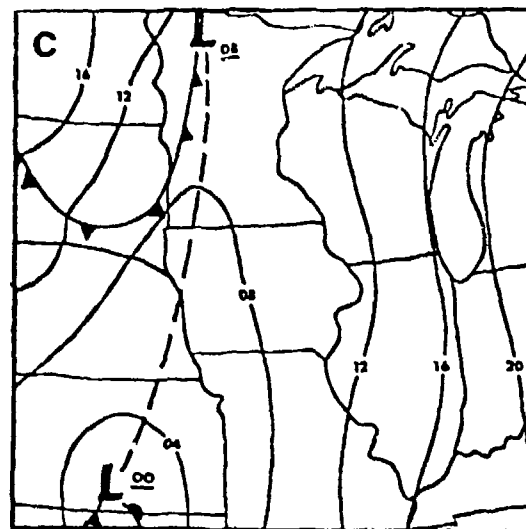


Figure 17: Same as Figure 2 except for (a) 1200 GMT 31 January 1981, (b) 1800 GMT 31 January 1981 and (c) 0000 GMT 1 February 1981.



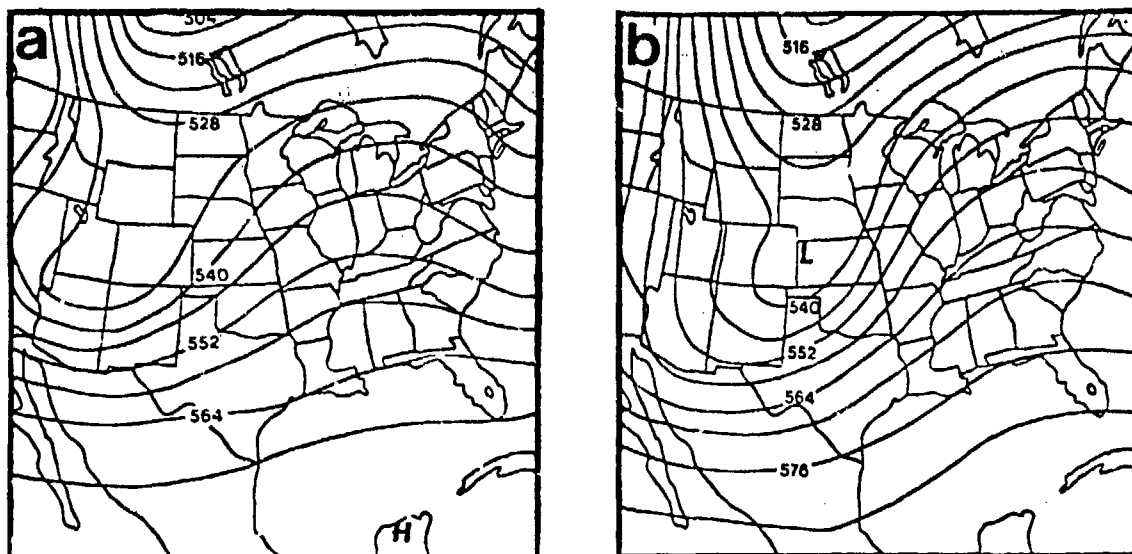


Figure 18: Same as Figure 3 except for (a) 1200 GMT 31 January 1981 and (b) 0000 GMT 1 February 1981.

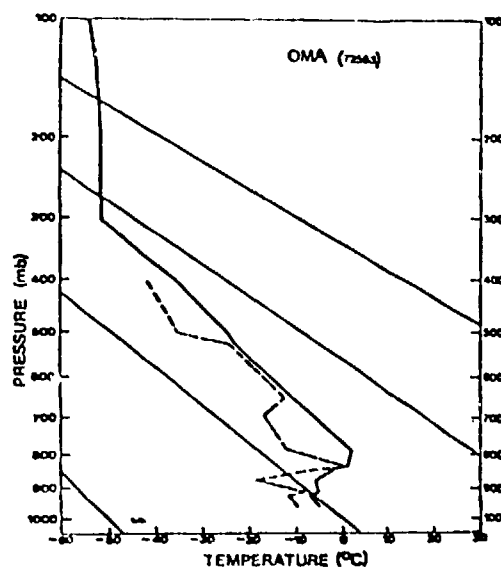


Figure 19: Same as Figure 4 except for Omaha, Nebraska, 1200 GMT 31 January 1981.

a)

DDHHMM	STN	T	TD	WIND	PRES	LO	MID	HI	VIS	WX	PCPN
061200	CAK	-8	-12	3008	1021.6	3	0	0	10	SW-	
061200	IAG	-8	-13	1012	1023.3	3	0	0	10	S-	
061200	PAK	-3	-6	0805	1016.5	3	0	0	8	S-	
061200	EKN	-3	-7	1503	1015.8	3	0	0	4	S-	
061200	SHD	-3	-62	1805	1018.5	3	0	0	1.5	S-F	
061200	CAW	-3	-8	1304	1016.8	3	0	0	7	S-	
061200	HTS	-3	-6	1209	1015.5	3	0	0	5	S-	0.06
061200	HNW	-5	-6	1407	1013.4	3	0	0	2.0	S-	0.01
061200	BLF	-6	-6	1305	1013.8	3	0	0	3	S-F	0.03
061200	LYH	-3	-4	1603	1019.2	3	0	0	1.5	S-F	0.01
061200	ROA	-3	-3	1506	1018.2	3	0	0	2.0	S-	0.04
061200	DAN	-3	-4	0000	1019.9	3	0	0	1.5	S-	0.99
061200	TRI	-4	-5	0000	1015.5	3	0	0	1.5	S-F	0.08
061200	GSD	-3	-4	0905	1018.5	3	0	0	2.0	S-F	0.07
061200	INT	-2	-4	0803	1017.8	3	0	0	0.7	S-F	
061200	HNY	-2	-4	1305	1017.5	3	0	0	1.5	S-	
061200	AVL	-3	-3	1805	1014.8	3	0	0	7	S-	0.12
061200	RIU	-3	-3	0000	1020.2	3	0	0	0.7	S-F	0.06
061200	FAY	-1	-2	1204	1020.9	3	0	0	0.5	S-	
061200	CLT	-1	-2	1405	1017.8	3	0	0	1.0	S-F	0.15
061200	GSP	-1	-2	0000	1017.2	3	0	0	1.0	S-F	0.93
061200	FLC	-2	-2	0305	1018.5	3	0	0	0.5	S-	
061200	ILM	1	-1	0210	1019.2	3	0	0	3	S-	0.05
061200	CAE	-1	-1	0603	1018.9	3	0	0	0.5	S-	0.23
061200	LWB	-5	-9	0000	1016.1	3	0	0	3	S-	
061200	CKB	-5	-6	3501	1016.8	3	0	0	1.0	S-	
061200	RLI	-2	-6	1108	1021.6	3	0	0	7	S-	
061200	AGS	0	-1	0403	1017.5	3	0	0	2.5	S-	0.42
061200	APN	-12	-13	0104	1023.9	2	3	0	10	SW-	
061200	GRN	-8	-10	0310	1023.6	3	0	0	5	S-	0.01
061200	MKG	-8	-11	0710	1020.9	3	0	0	7	S-	0.03
061200	HNE	-3	-6	0613	1020.2	3	0	0	6	S-F	0.10
061200	HSN	-8	-9	0114	1020.5	3	0	0	5	S-	0.07
061200	AZO	-7	-10	0508	1018.9	3	0	0	3	S-	
061200	MWC	-3	-62	0810	1020.5	3	0	0	1.0	S-	
061200	RTL	-9	-9	0510	1018.5	2	0	0	5	S-	
061200	ORF	-3	-6	0909	1017.8	3	0	0	5	S-F	0.02
061200	DPA	-5	-62	0610	1017.8	3	0	0	4	S-	
061200	MDW	-4	-6	0713	1019.2	3	0	0	3	S-	
061200	RFD	-3	-6	0211	1018.9	3	0	0	2.0	S-	0.04
061200	SEN	-4	-7	0710	1017.5	3	0	0	4	S-F	0.01
061200	FWA	-6	-10	0614	1016.5	3	0	0	4	S-	0.08
061200	TOL	-6	-8	0611	1018.9	3	0	0	4	S-	0.01
061200	FDY	-6	-7	0709	1017.5	2	0	0	2.0	S-	
061200	MFD	-4	-62	0606	1016.5	3	0	0	5	SW-	0.21
061200	LAF	-3	-6	0509	1015.5	3	0	0	2.0	S-	0.06
061200	PIA	-5	-6	0204	1016.5	3	0	0	3	S-F	0.02
061200	UTN	-5	-9	3220	1018.5	3	0	0	4	S-	0.01
061200	CHI	-5	-7	3005	1014.1	3	0	0	2.0	S-	
061200	IND	-2	-4	0807	1013.8	3	0	0	2.0	S-F	0.04
061200	DAY	-4	-7	0910	1015.1	3	0	0	1.5	S-	

b)

DDHHMM	STN	T	TD	WIND	PRES	LO	MID	HI	VIS	WX	PCPN
061200	RIU	-3	-3	0000	1020.2	3	0	0	0.7	S-F	0.06
061300	RIU	-2	-	0501	1020.2	3	0	0	0.7	S-F	
061400	RIU	-	-	0904	1019.2	3	0	0	0.3	S	
061500	RI	-	-	0804	1018.5	3	0	0	0.8	S-F	0.08
061600	RIU	-1	-2	0605	1017.8	3	0	0	0.7	S-F	
061700	RIU	0	-1	0304	1016.8	3	0	0	0.7	S-F	
061800	RIU	-1	-2	0606	1015.5	3	0	0	0.8	S-F	0.16
061900	RIU	0	-2	0406	1014.8	3	0	0	1.6	S-F	
062000	RIU	0	-2	0406	1014.5	3	0	0	0.8	S-F	
062100	RIU	0	0	3607	1014.5	3	0	0	2.7	S-F	

Figure 20: Example McIDAS listings of weather observations, 6 February 1980 for Raleigh-Durham, North Carolina.

a)

189	188	188	187	187	185	181	176	168	155	147	143	142	141	140	141	141	141
187	186	185	182	179	172	160	151	145	141	139	138	138	139	141	142	142	141
187	186	185	182	179	172	160	151	145	141	139	138	138	139	141	142	142	141
181	178	170	161	153	147	146	145	143	142	142	143	146	149	151	153	154	154
181	178	170	161	153	147	146	145	143	142	142	143	146	149	151	153	154	154
160	153	146	143	142	142	143	143	145	146	149	153	157	158	160	158	158	157
160	153	146	143	142	142	143	143	145	146	149	153	157	158	160	158	158	157
142	143	143	145	146	149	151	153	154	155	158	161	163	163	161	160	158	157
142	143	143	145	146	149	151	153	154	155	159	164	165	162	160	159	158	
150	154	155	150	152	154	154	155	158	160	162	163	166	167	170	164	162	160
152	154	155	154	154	155	157	160	163	165	164	165	166	165	163	163	161	159
150	152	153	153	153	154	154	159	159	160	160	163	162	163	161	161	160	157
160	163	164	166	157	155	152	155	155	157	157	154	154	149	145	139	137	136
160	162	164	162	158	153	154	154	154	155	155	153	152	147	145	138	136	134
161	161	163	165	159	152	152	151	151	149	152	153	154	146	142	139	136	133
158	160	166	158	157	154	154	150	147	143	141	138	137	136	136	136	134	134
158	160	160	158	157	154	150	148	146	142	140	140	136	134	133	133	133	133
141	141	141	141	141	141	138	137	136	134	134	134	134	133	133	133	133	132

36nm

36nm

b)

MEAN BRIGHTNESS 151.5 SD 12.6 MEDIAN 153.5 MODE 155

Figure 21: (a) Sample digital IR brightness array (centered station is at x) with (b) mean, median, mode and standard deviation of values.

189	188	188	187	187	185	181	176	168	155	147	143	142	141	140	140	141	141
187	186	185	182	179	172	160	151	145	141	139	138	138	139	141	142	142	141
187	186	185	182	179	172	160	151	145	141	139	138	138	139	141	142	142	141
181	178	170	161	153	147	146	145	143	142	142	143	146	149	151	153	154	154
181	178	170	161	153	147	146	145	143	142	142	143	146	149	151	153	154	154
160	153	146	143	142	142	143	143	145	146	149	153	157	158	160	158	158	157
160	153	146	143	142	142	143	143	145	146	149	153	157	158	160	158	158	157
142	143	143	145	146	149	151	153	154	155	158	161	163	163	161	160	158	157
147	143	143	145	146	149	151	153	149	154	159	159	164	165	162	160	159	158
150	154	155	150	152	154	154	155	149	154	159	159	164	165	162	160	159	158
152	154	155	154	154	155	157	157	163	163	164	165	166	165	163	163	161	159
150	152	153	153	153	154	154	159	159	160	160	163	162	163	161	161	160	157
160	163	164	160	157	155	155	155	157	157	154	154	149	145	139	137	136	136
160	162	164	162	158	153	154	154	154	155	155	153	152	147	145	138	136	134
161	161	163	165	159	157	152	151	151	149	152	153	154	146	142	138	136	133
158	160	160	158	157	154	154	150	147	143	141	138	137	136	136	136	134	134
158	160	160	158	157	154	150	148	146	142	140	140	136	134	133	133	133	133
141	141	141	141	141	138	137	136	134	134	134	134	134	134	133	133	133	132

149	154
156	160

$$X = \frac{149 + 154 + 156 + 160}{4} = 154$$

Figure 22: Example of point brightness calculation (for station at x).

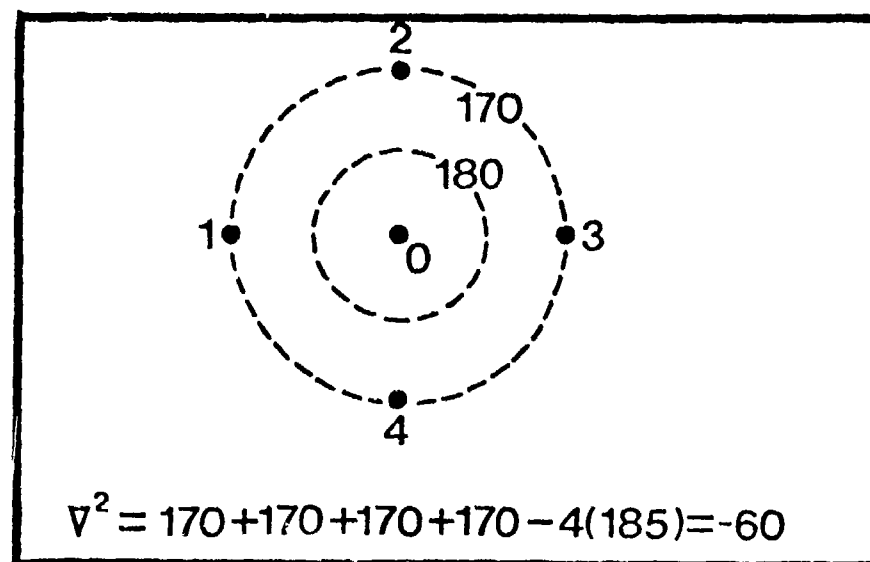
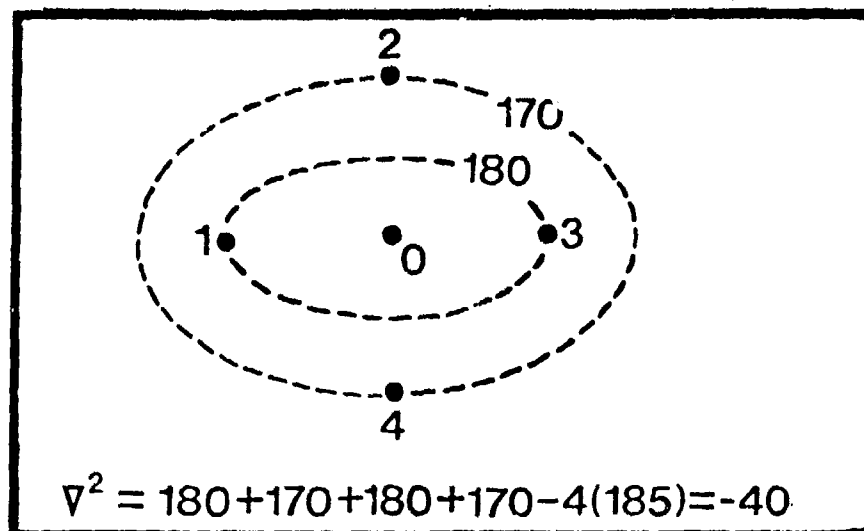


Figure 23: Example showing magnitude dependency of Laplacian values upon the "circularity" of relative maxima or minima.

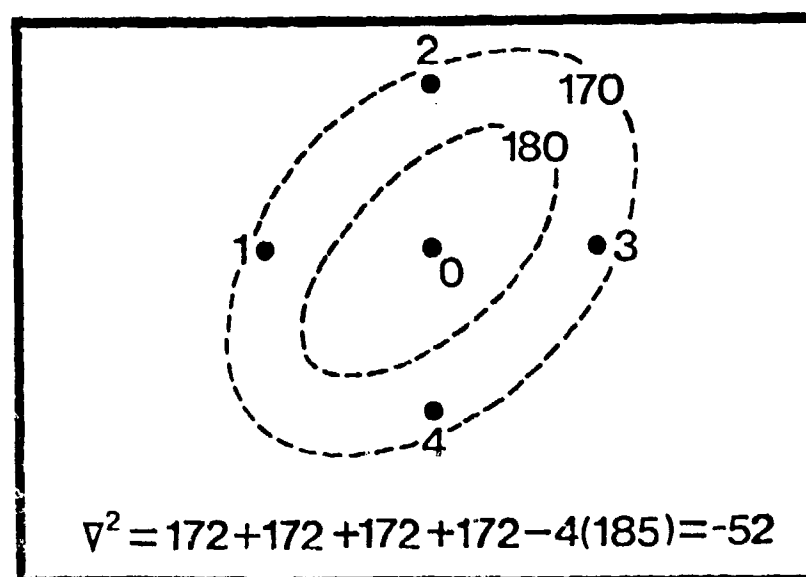
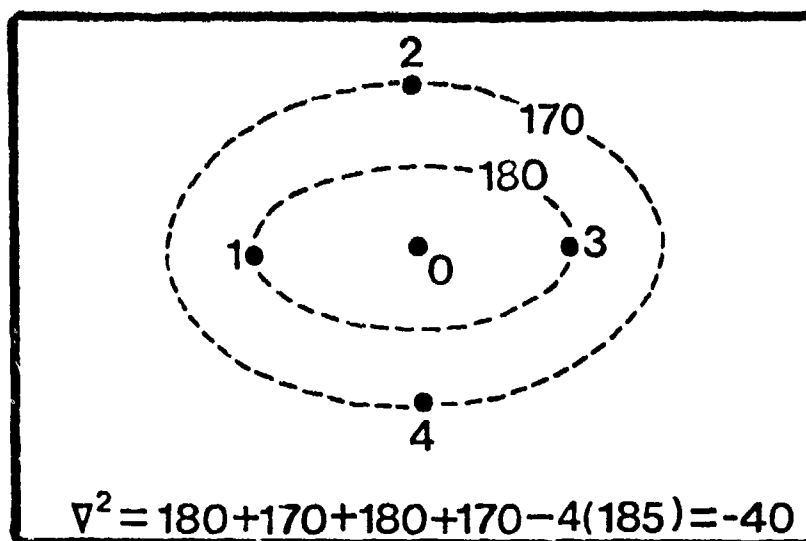


Figure 24: Example showing dependency of Laplacian values upon the orientation of banded maxima or minima.

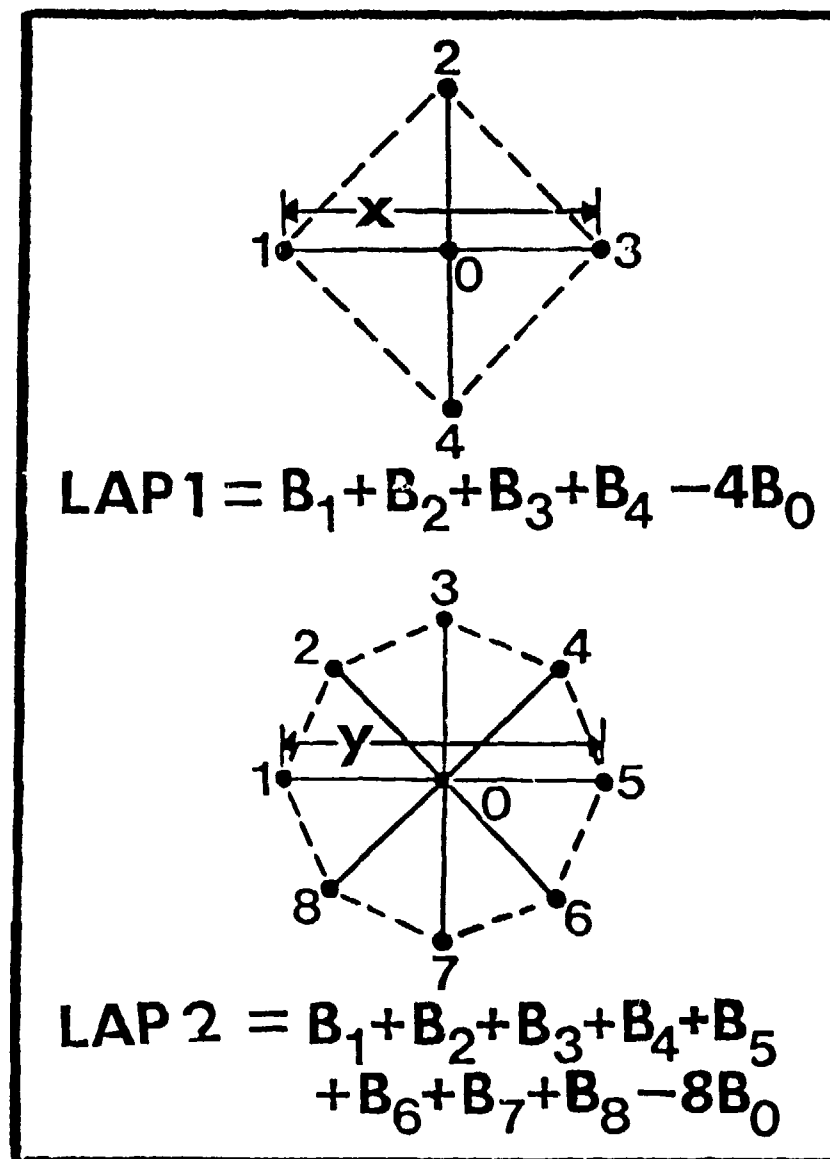


Figure 25: Schematic of five-point Laplacians (ILAP1 and OLAP1) and nine-point Laplacians (ILAP2 and OLAP2) including equations used for calculations (x and y are 16 nm or 32 nm).

STATION MSN CASE 1

HOUR	VIS	WX	DM	ILAPI	OLAPI	ILAP2	OLAP2
18Z	1.5	S-	-20	+36	+104	+30	+108
19Z	0.5	S	+5	-19	-31	-22	-23
20Z	0.5	S	+1	+3	-7	+2	-7
21Z	0.7	S-	-2	+6	+6	+6	+5

Figure 26: Tabulation format for hourly values of visibility, weather and all five parameters (sample data for Madison, Wisconsin from 14 April 1980 case).

INTENSITY INCREASES

Δ VIS	Δ DM	Δ ILAPI	Δ OLAPI	Δ OLAPI	Δ ILAP2

Figure 27: Tabulation format for hourly changes in visibility and all five parameters (example for intensity increases).

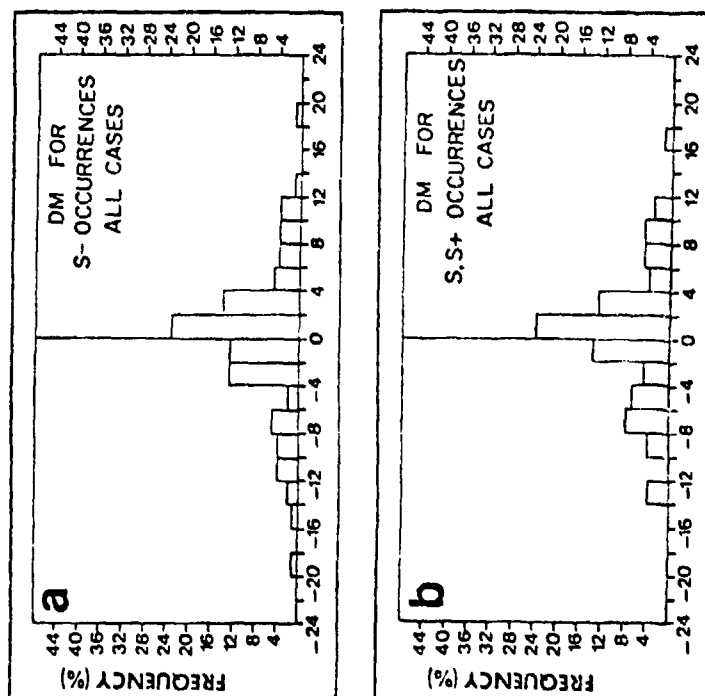


Figure 28: Interval frequency distributions of DM values for (a) light and (b) moderate, heavy snowfall occurrences (all cases).

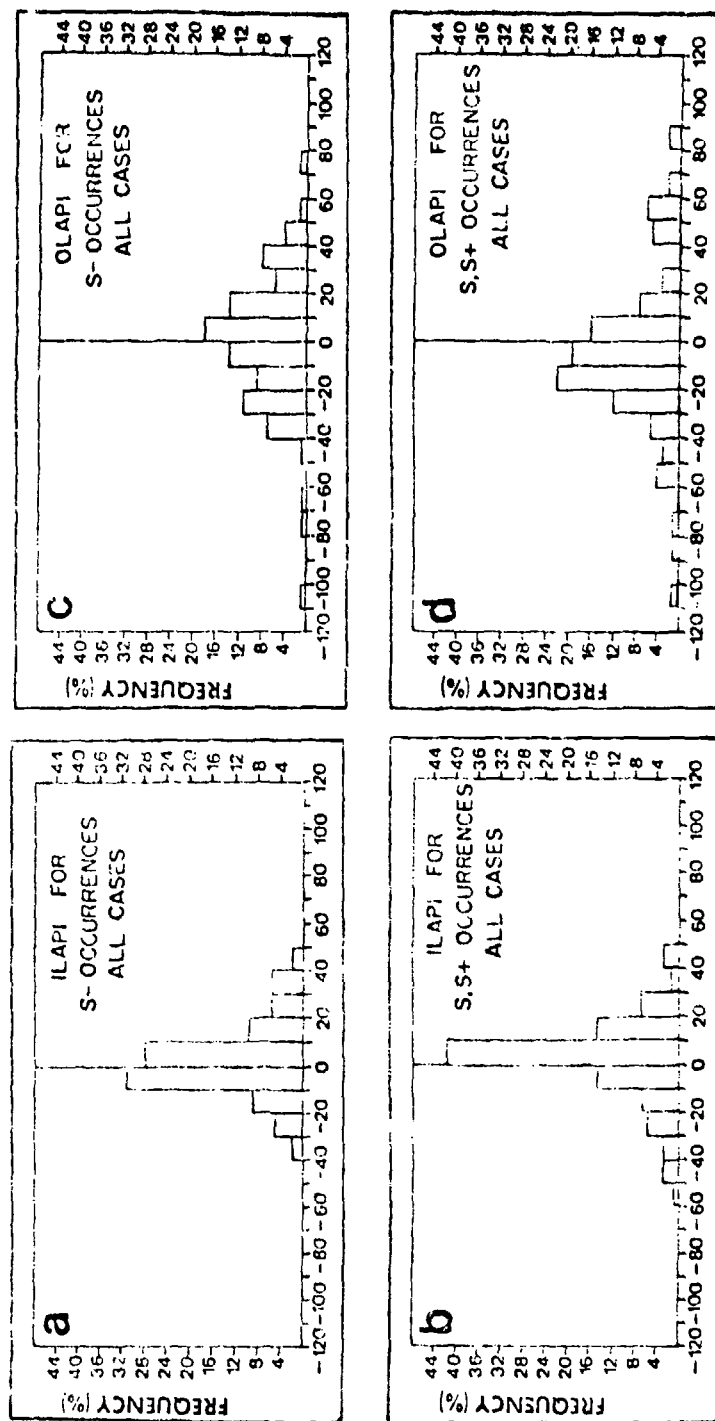


Figure 29: Same as Figure 28 except for (a, b) ILAPI and (c, d) OLAPI.

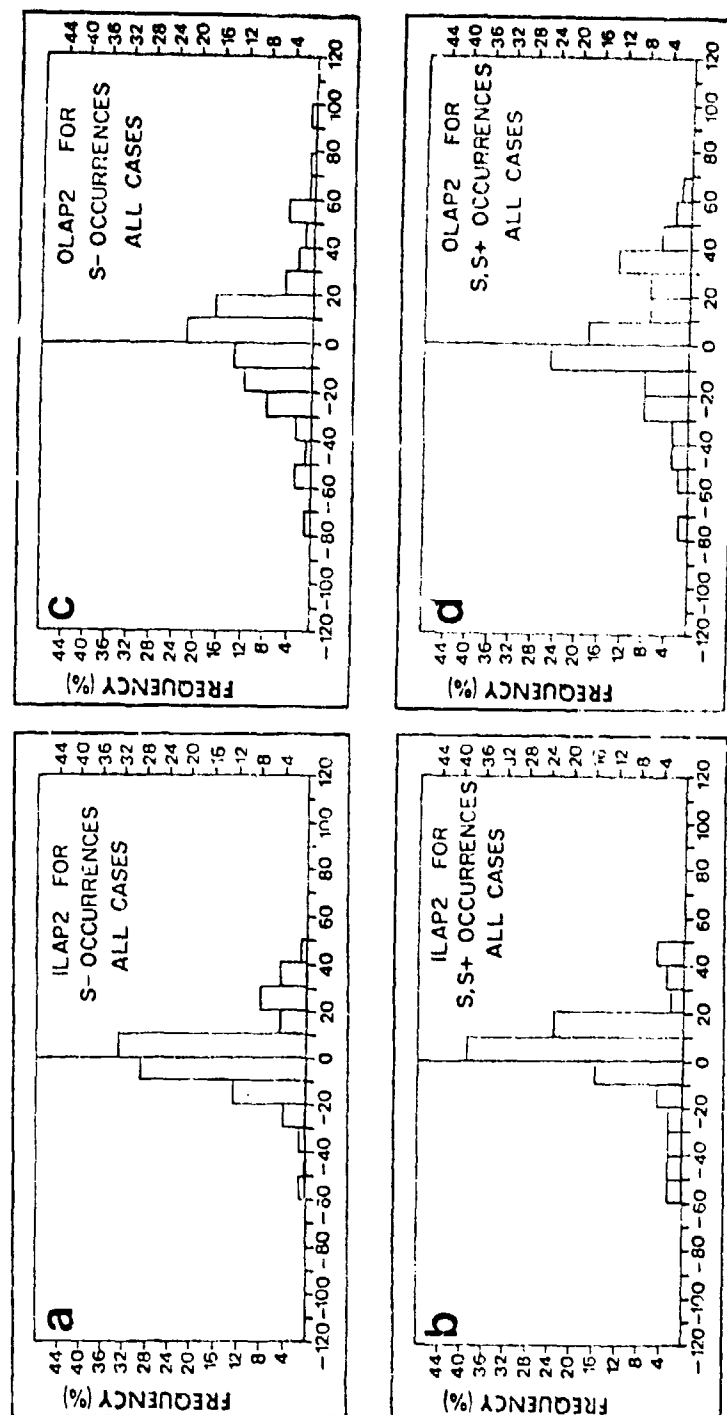


Figure 30: Same as Figure 28 except for (a, b) ILAP2 and (c, d) OLAP2.

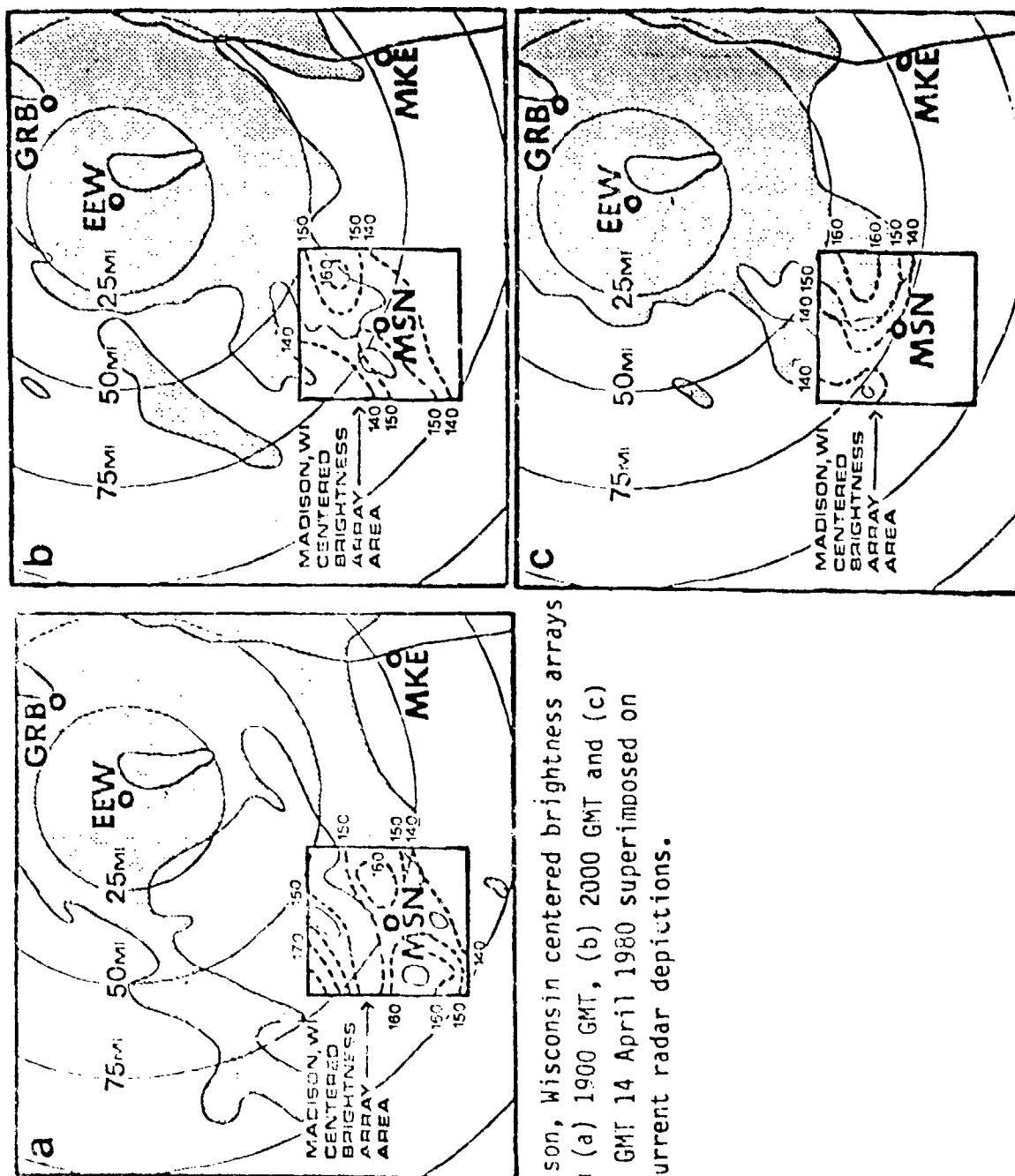


Figure 31: Madison, Wisconsin centered brightness arrays from (a) 1900 GMT, (b) 2000 GMT and (c) 2100 GMT 14 April 1980 superimposed on concurrent radar depictions.

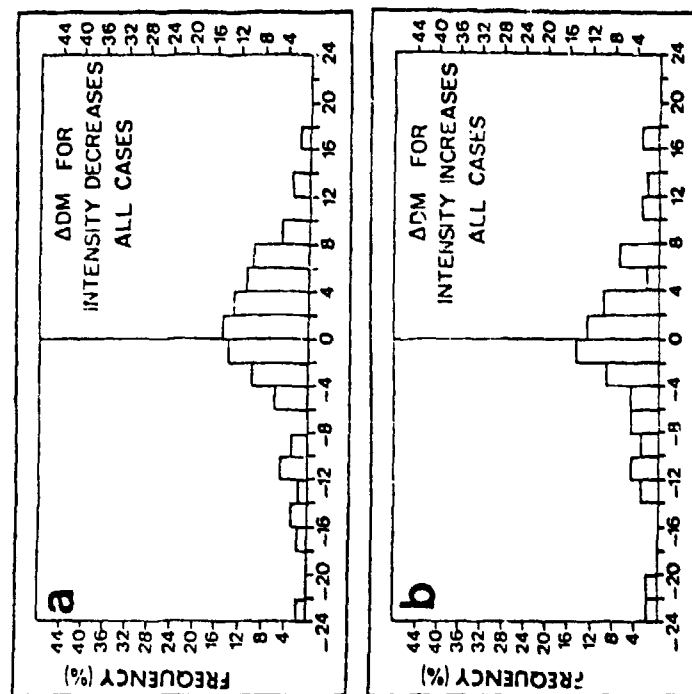


Figure 32: Interval frequency distributions of ADM values for (a) intensity decreases and (b) intensity increases (all cases).

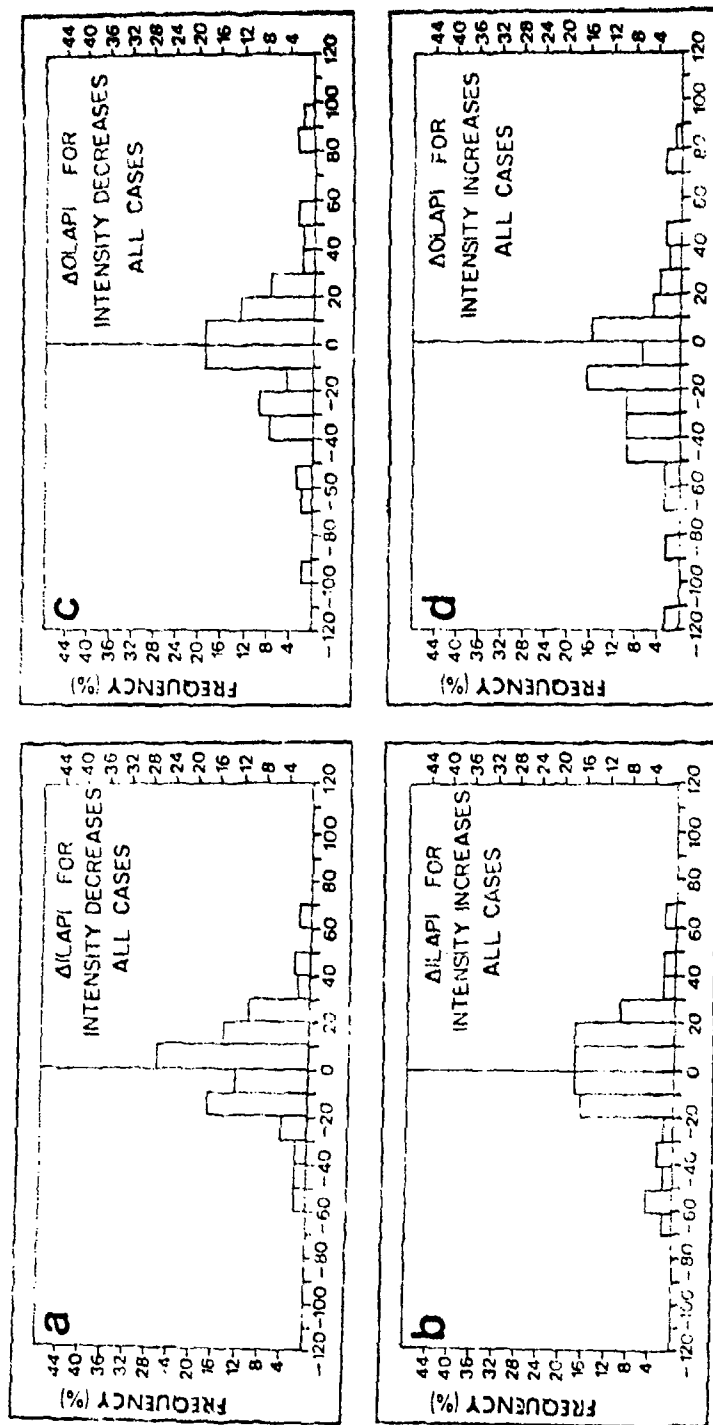


Figure 33: Same as Figure 32 except for (a, b) $\Delta ILAP1$ and (c, d) $\Delta OLAP1$.

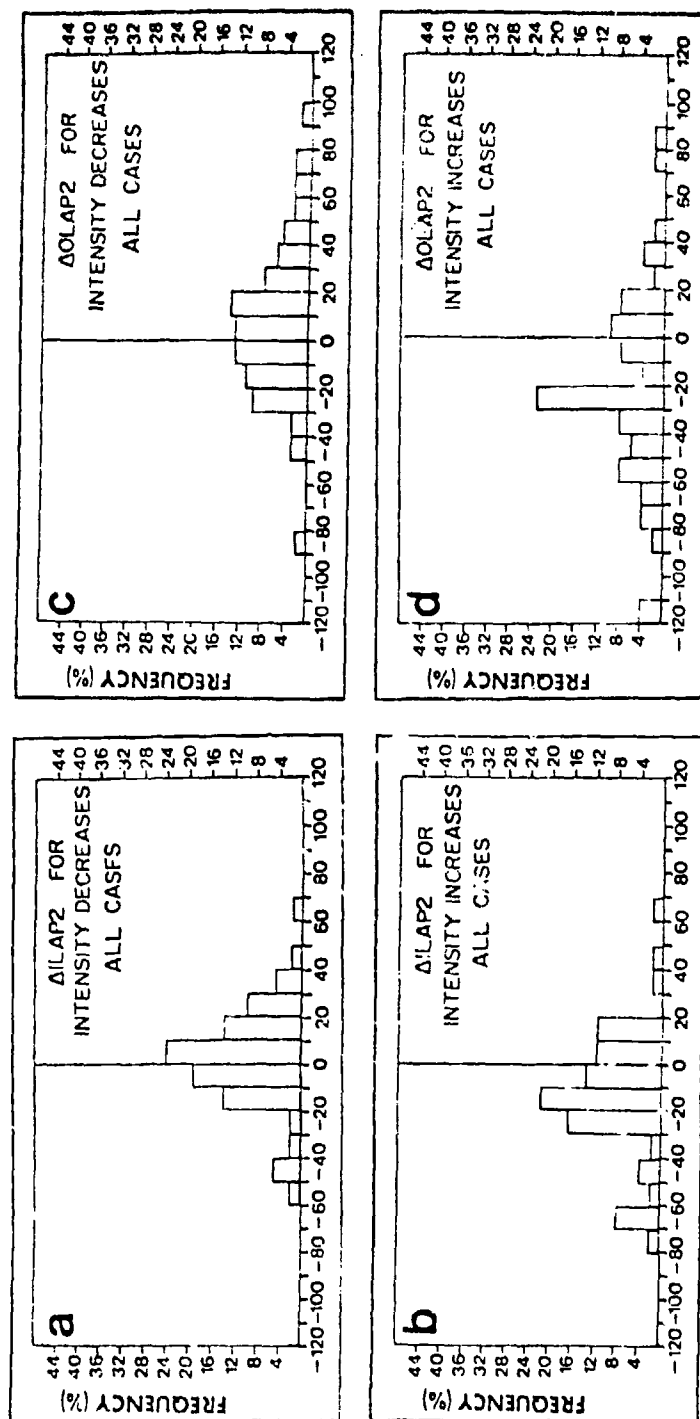


Figure 34: Same as Figure 32 except for (a, b) $\Delta ILAP2$ and (c, d) $\Delta OLAP2$.

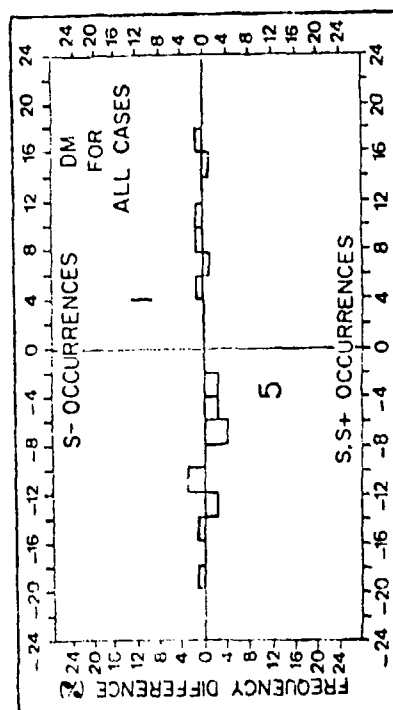


Figure 35: Interval frequency difference distribution of DM, including subtotal frequency differences for positive and negative intervals, for light and moderate, heavy snowfall occurrences.

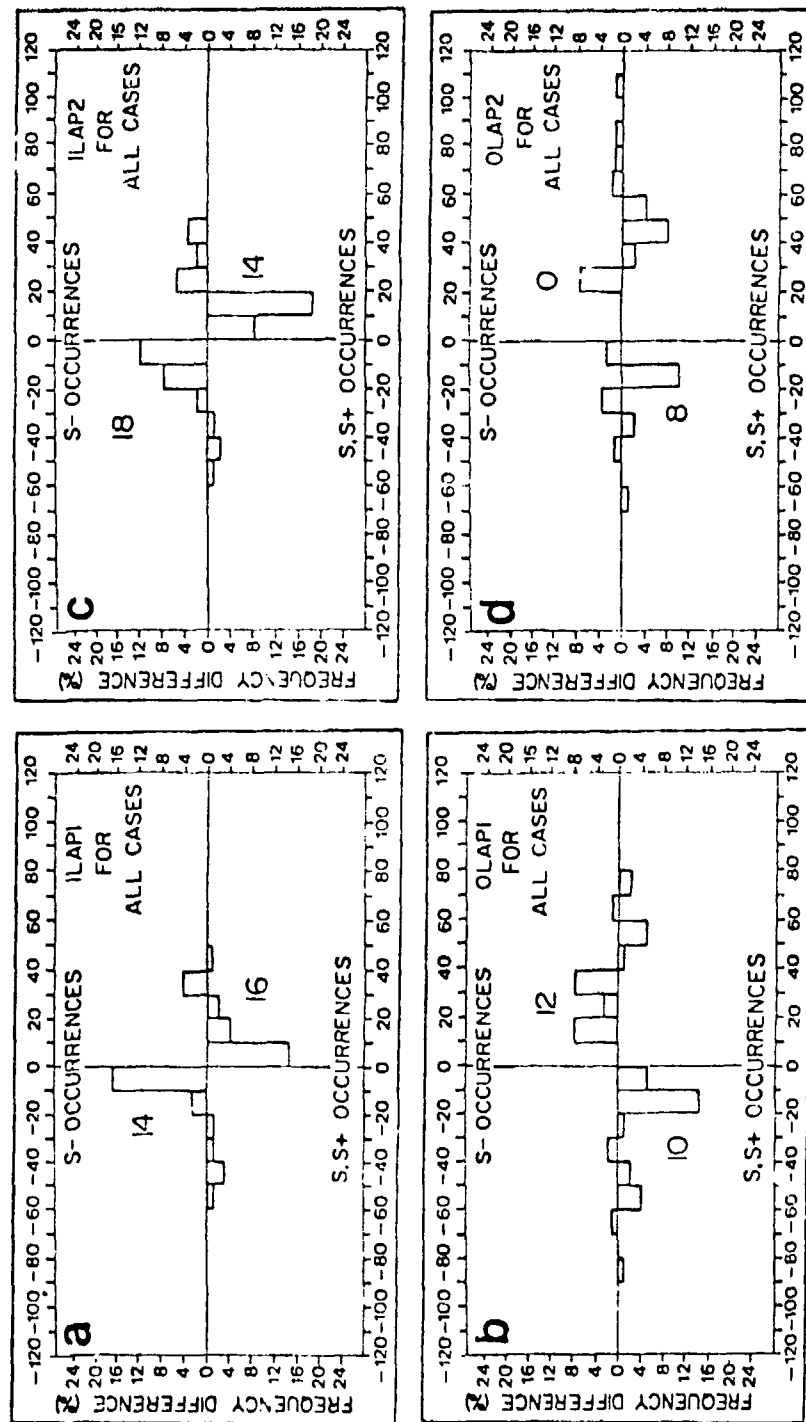


Figure 36: Same as Figure 35 except for (a) ILAP1, (b) OLAP1, (c) ILAP2, and (d) OLAP2.

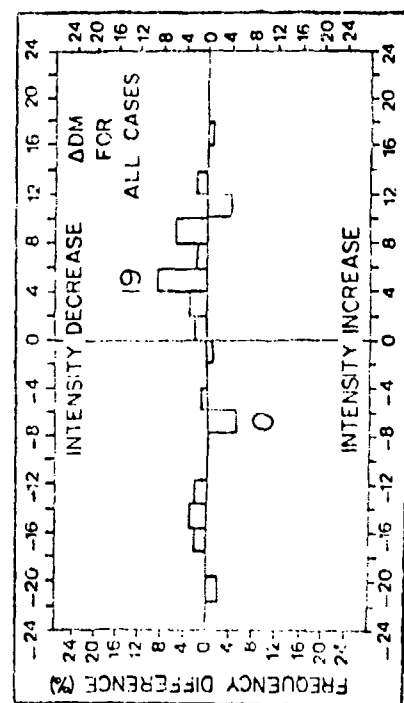


Figure 37: Interval frequency difference distribution of ADM for intensity decreases and intensity increases. See Figure 35 for format.

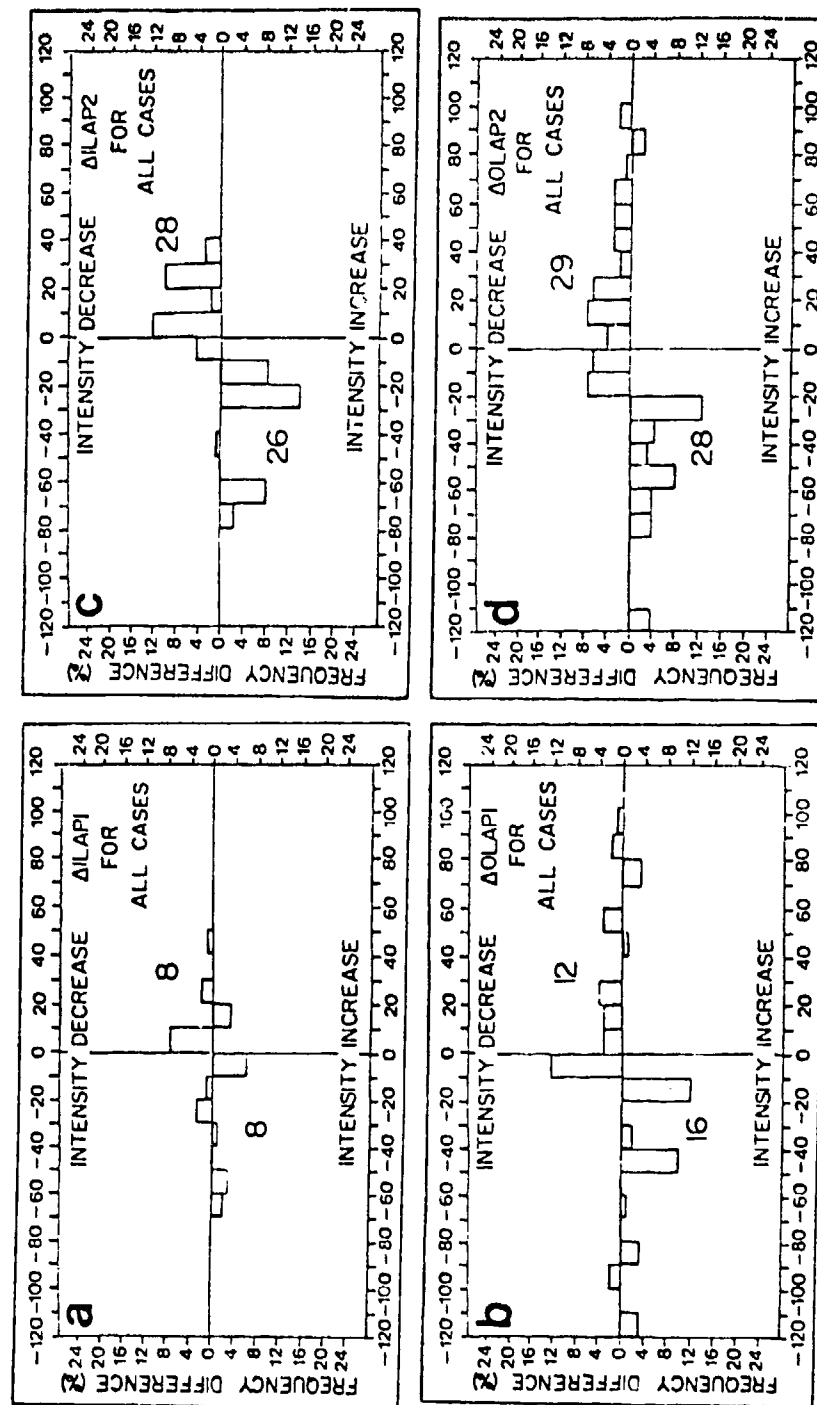


Figure 38: Same as Figure 37 except for (a) $\Delta ILAP1$, (b) $\Delta OLAP1$, (c) $\Delta ILAP2$ and (d) $\Delta OLAP2$.

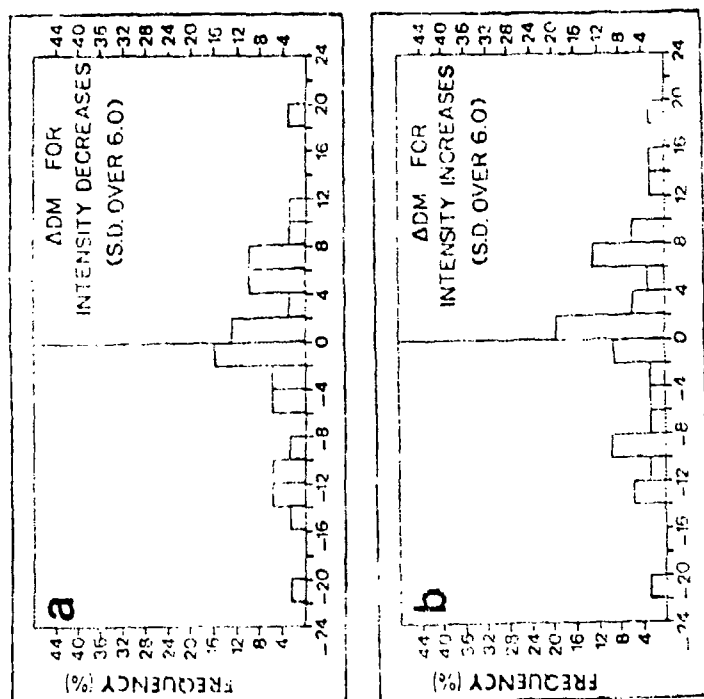


Figure 39: Interval frequency distributions of ΔM for (a) intensity decreases and (b) intensity increases for special 50 array subset.

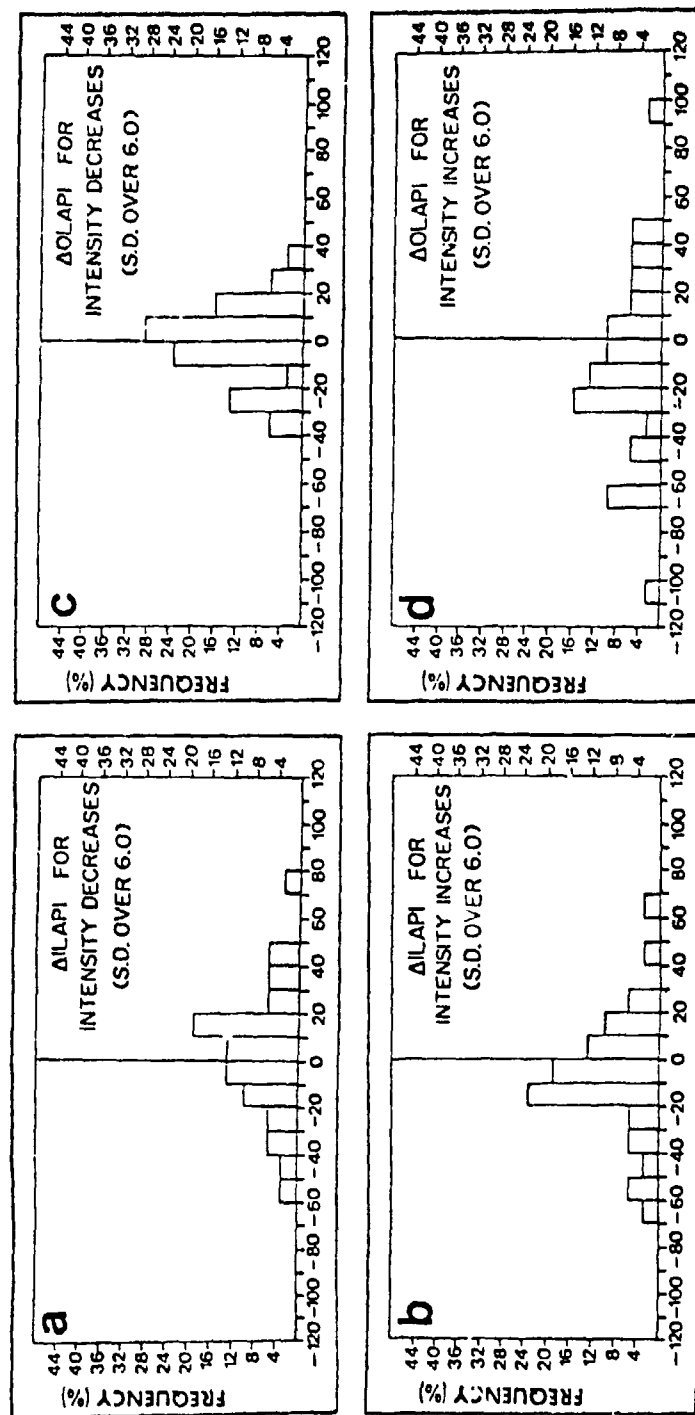


Figure 40: Same as Figure 39 except for (a, b) $\Delta ILAPI$ and (c, d) $\Delta OLAPI$.

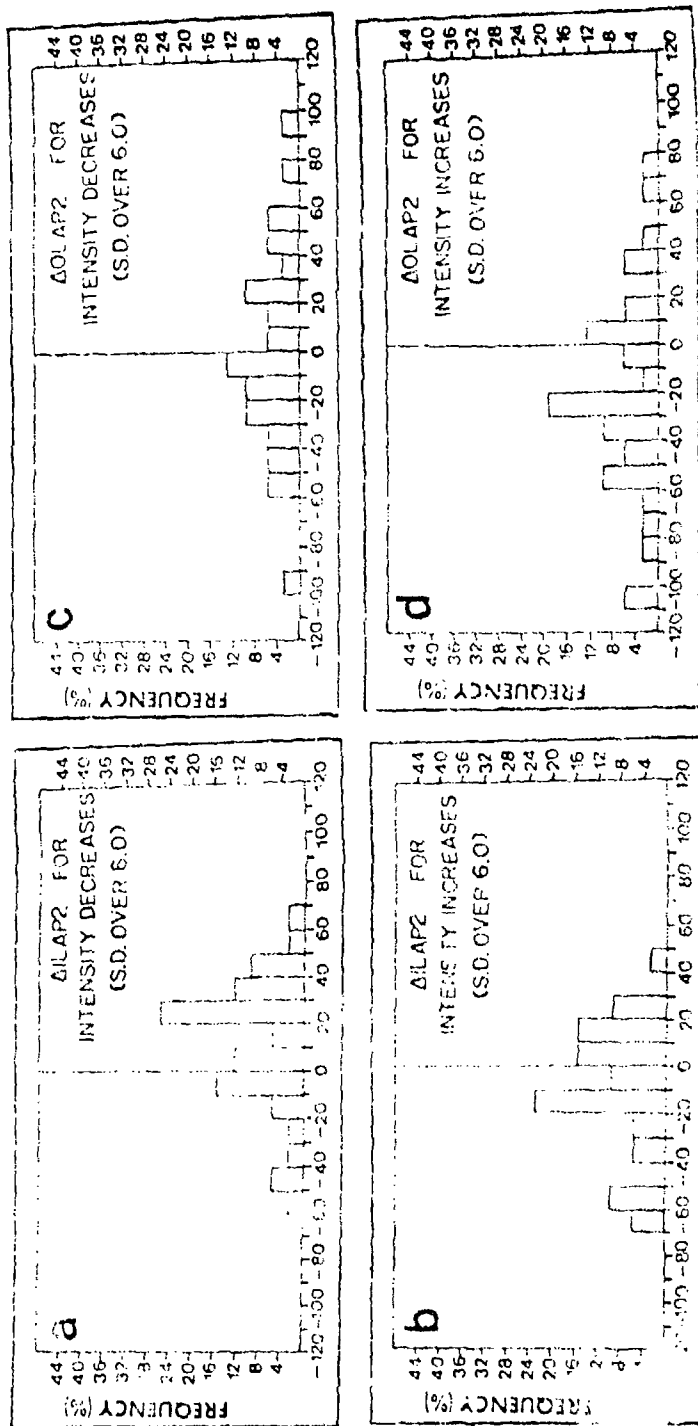


Figure 41: Same as Figure 39 except for (a, b) Δ ILAP2 and (c, d) Δ OLAP2.

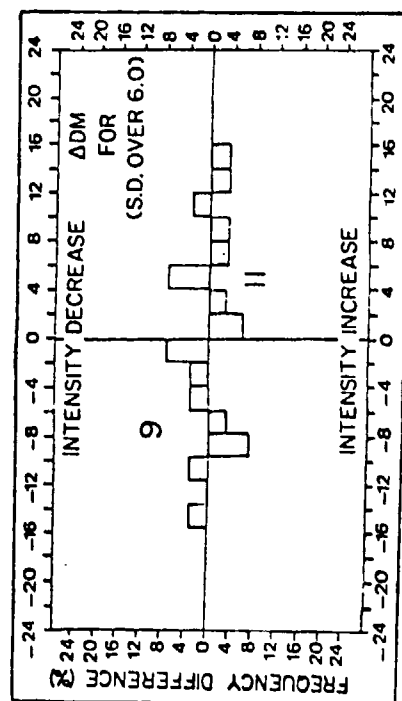


Figure 42: Same as Figure 37 except for special 50 array subset.

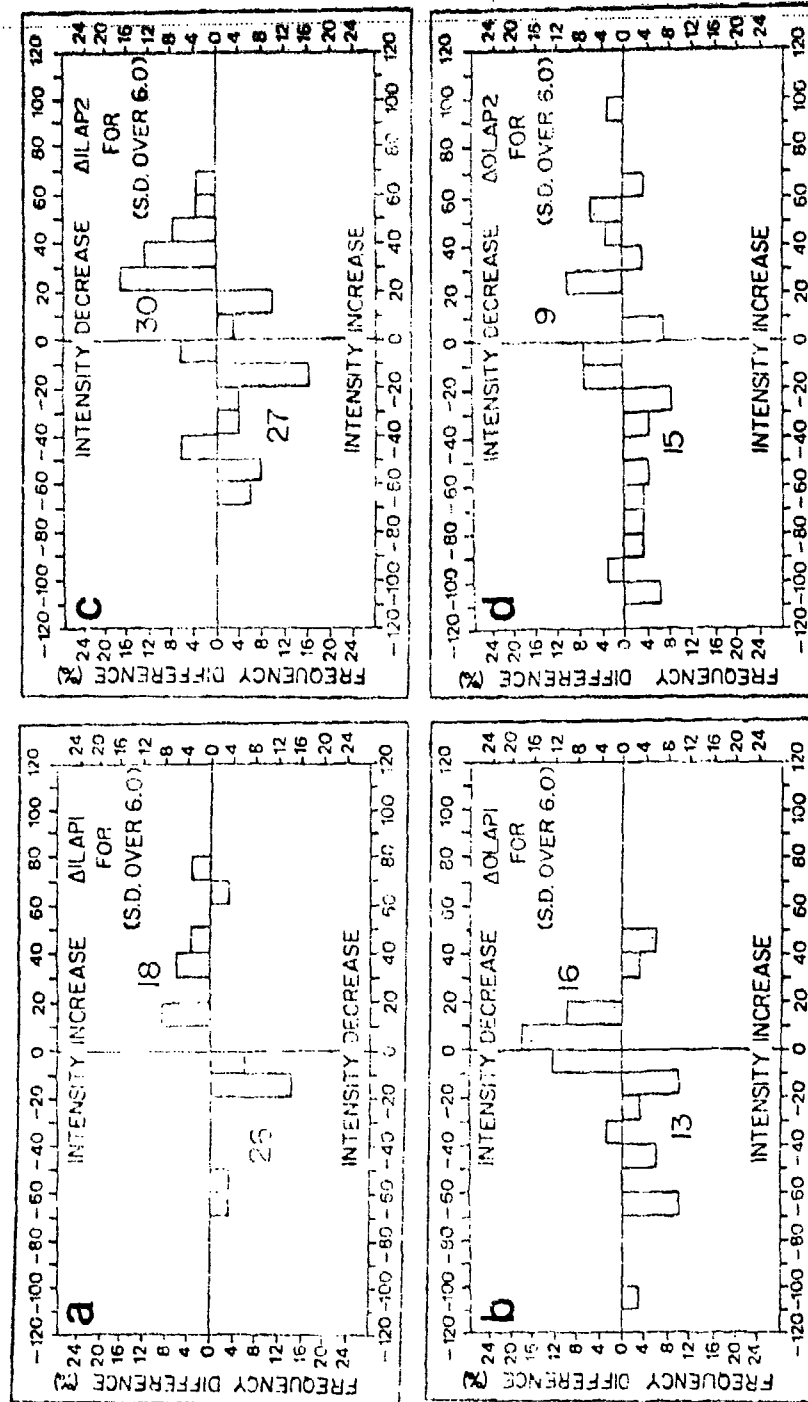


Figure 43: Same as Figure 42 except for (a) $\Delta ILAP1$, (b) $\Delta OLAP1$, (c) $\Delta ILAP2$ and (d) $\Delta OLAP2$.